The Influences of Forest Fires Inducted Albedo Differences on the Generation of Mesoscale Circulations

by
Captain John B. Knowles

Department of Atmospheric Science
Colorado State University
Fort Collins, Colorado

Roger A. Pielke, Advisor

Colorado State University

Department of Atmospheric Science

Paper No. 527

THE INFLUENCE OF FOREST FIRE INDUCED ALBEDO DIFFERENCES ON THE GENERATION OF MESOSCALE CIRCULATIONS

Captain John B. Knowles

Department of Atmospheric Science
Colorado State University
Fort Collins, Colorado
Summer 1993

Atmospheric Science Paper No. 527

ABSTRACT

THE INFLUENCE OF FOREST FIRE INDUCED ALBEDO DIFFERENCES ON THE GENERATION OF MESOSCALE CIRCULATIONS

The development of a mesoscale circulation by the thermal contrast between a fire burned area surrounded by untouched vegetation was simulated by the Regional Atmospheric Modeling System (RAMS) in order to show the circulation's ability to generate clouds and precipitation. The simulations used two fires that occurred during the summer of 1988. The first fire was over 400 square kilometers in size, while the second fire was over 100 square kilometers in size.

Results of the 8-hour simulations showed that the thermal differences between the first fire burn area and surrounding unburned area generated a well-developed mesoscale circulation with a vertical updraft speed of over 3.5 m s^{-1}. The simulation also developed clouds and precipitation directly above the circulation center. Simulation of the second fire burn area generated a mesoscale circulation with a vertical updraft speed of over 2.5 m s^{-1}. Although the second simulation did develop clouds and some very light precipitation, it could not be directly tied to the mesoscale circulation itself.

Sensitivity runs studying the effects of burn area size, albedo, geostrophic wind speed and direction, and thermodynamic stability were also run. Results showed that the strongest circulation centers developed over areas with the largest burns (400 square kilometers) and albedo differences (0.15 for the unburned area, 0.05 for the burned area), along with light synoptic flow ($\leq$ 2.5 m s^{-1}) and a weakly stratified atmosphere ($\frac{\partial \theta}{\partial z}$ = 2.5°C km^{-1}). The lightning plots showed that most lightning strikes occurred over higher terrain. But, there were also clusters of lightning strikes near the burn areas in the river valley.

This, along with the prevailing south-westerly surface winds, showed that convection could be generated in and near the fire burned areas.

The simulations showed that it is possible for the thermal differences between fire burned areas and the surrounding unburned areas to generate a mesoscale circulation of sufficient strength to develop clouds, precipitation, and possible lightning. Possible results of the increased convection would be more lightning, more lightning ignited fires, more burned landscape, and modified precipitation patterns.

Captain John B. Knowles
Department of Atmospheric Science
Colorado State University
Fort Collins, Colorado 80523
Summer 1993

ACKNOWLEDGEMENTS

I'd like to thank my advisor, Dr. Roger Pielke for his support and many helpful contributions over the past 21 months. His suggestions on how and where to find support for this project was a major contributing factor to it's completion. I would also like to thank committee members Drs. Thomas McKee and natural resource scientist William Parton for their help and contributions to this thesis. A special thanks to forestry scientist John Yarie (University of Alaska) for the countless hours that he put in developing lightning strike plots and forest fire location maps. This paper would not have been possible without the data provided by John.

I would also like to acknowledge several members of Drs. Pielke and William Cotton for assisting with the many questions that I had on RAMS. Jeff Copeland, Joe Eastman, Cathy Finley, John Lee, and Greg Thompson were always willing to listen and provide answers on the workings of RAMS. I just hope that I didn't come across with the intelligence of the average rock when I asked those questions. Drs. Craig Tremback and Bob Walko are also thanked for their suggestions and help.

Captains Tony Leute and Bruce VanAartsen, along with Matt Savoie, Dave Mocko, and Jeff Copeland are thanked for their stress relieving assistance at noon. My only regret was not giving the queen to Jeff more often. A special thanks to my roommates and fellow ski monsters, John Papineau and Greg Poulos, for putting up with me during my assignment here at CSU. A very special thanks to Captain Tony Leute for sticking with me during both the good and bad times. I only hope that I can be around to help him if he needs it. I wish both Tony and Tara the best of luck in the future. I would also like to thank Dallas McDonald for her part in the typing of this paper, along with pestering me for monthly progress reports. Her expertise in word processing was invaluable. Bryan

Critchfield an Tony Smith are also thanked for their assistance on this and many other projects. Judy Sorbie-Dunn assisted on drafting many of the figures.

Finally, I'd like to thank both the Air Force and my wife, Mindy, for their support in this endeavor. The Air Force for allowing me the chance to attend Colorado State and do something that I have always wanted to do, and my wife for putting up with my ranting and raving during first year classes and my frustration and confusion during the second year. Her support was always there and it is and will always be appreciated. One thing though, no more cats.

The modeling simulations were completed on an IBM RISC workstation provided by the National Park Service. RAMS was developed under support of NSF and ARO. This research was made possible by the United States Air Force. Data on forest fires, lightning, and winds was provided via the University of Alaska.

TABLE OF CONTENTS

LIST OF FIGURES

LIST OF TABLES

Chapter 1

INTRODUCTION

1.1 Overview

The initialization of a mesoscale circulation may be caused by several forcing mechanisms, including thermal contrasts, with the most commonly studied examples being sea breeze and mountain/valley flows. Less commonly studied, but also of importance are snow, island/ocean, and irrigation/dryland breezes. This thesis will study the mesoscale circulation initialized by the thermal contrast between a fire burned area surrounded by untouched vegetation. This mesoscale circulation can help to develop convective activity in the area, depending on the the burn area's size, existing weather conditions, topography, and time of day. It is possible to show the existence of the mesoscale circulation through the use of lightning network data, satellite imagery and follow up fires. Follow up fires are fires that occur close to the the mesoscale circulation ($\leq$50 km) and within a year after the original fire.

Fires are a part of life in the western part of the United States and Canada, and the interior of Alaska. These fires can cost millions of dollars to extinguish, destroy thousands of acres of timber, imperil entire watersheds and animal habitats, and cause tremendous damage to valuable recreational resources (Morris, 1934). Roughly 50 percent of the fires in the Anchorage and Fairbanks areas are caused by lightning strikes (Komarek, 1976). The other 50 percent are man-caused. In the wilderness, the percentage of lightning-caused fires is much higher. Man-caused fires start earlier in the year; mid-March and peak in mid-May, with a smaller peak in mid-June, and end in mid-September. Lightning fires start in early May, peak in mid-June, and end in mid-September. The reason that man-caused fires start earlier is that man starts moving around the interior by mid-March. Lightning-caused

fires cannot start until most of the snow cover is gone and moist convection processes can begin, usually by early May. This is a time of peak ignition for lightning (Flannigan et al., 1991). The forest floor at this time is covered by dead, and sometimes dry, organic material, an excellent medium for fire spread. Mid-season peaks in man-caused fires are attributed to a peak in the number of people (i.e., hunters, hikers, construction workers) out in the wilderness. The mid-season peak in lightning-caused fires is attributed to mid-June being the peak time for moist convection. The man-caused fires are normally very small (under 100 acres), due to most fires being set in the vicinity of towns, lakes, and major roads (Rowe, 1976). Lightning fires, on the other hand, occur almost anywhere, and can be up to several hundred thousand acres in size.

Lightning, the chief agent of ignition, is produced by moist convection (Rowe, 1976). Three mechanisms that contribute to moist or cumulus convection are:

1. Forced airflow over changes in elevation, mostly orographic effects.

2. Frontal activity; the interaction between cold and warm air.

3. Solar heating of terrain.

It is this third method that this study will concentrate on, although mechanisms 1 and 2 can also play a role. The lightning-induced fires cause burn areas ranging from a few acres to a few hundred square kilometers. The burn area, consisting of blackened tree stands and blackened organic surface matter, will have a lower albedo than the surrounding unburned environment (Viereck, 1979). This albedo difference will typically last for 1-3 years after the event, after which significant surface growth will reduce the albedo difference to negligible values. The difference in albedo between the two areas is of significance to the production of a mesoscale circulation. This is through the enhancement of vertical heat fluxes (Rodriguez, 1992). As mentioned above, this circulation can lead to the development and/or enhancement of convection. This convection can then produce lightning that could set off additional fires in the surrounding environment. The storms that produce lightning in Alaska typically have a cloudtop ranging from 8,000 to 12,000 meters in height, and are most active from late morning to late afternoon (Baughman, 1977). The topics covered in this work are briefly summarized in the following outline.

1.2 Summary

Chapter 2 presents a brief literature review of the various types of secondary circulations. These include sea breezes, snow breezes, island-ocean breezes, urban heat island breezes, and irrigation/dry land circulations. Additional information on forest fires and their effects on the environment will also be discussed. A brief description of the numerical model used in the study will be discussed in Chapter 3. This will include basic equations, numerical methods, and physical parameterizations used. Chapter 4 contains the actual model simulations used for the study. Model input along with actual results will be discussed there. Sensitivity runs involving changes in the variables used in Chapter 4 will be addressed in Chapter 5. This will include using differing values for thermodynamic stability, albedo, wind speed and direction, and burn size. Chapter 6 will discuss lightning network data. This will be tied together with results from Chapter 4 to validate the conclusions derived from the simulations. Finally, a summary of the conclusions reached in this study will be included in Chapter 7, along with a few suggestions for future research.

Chapter 2

LITERATURE REVIEW

2.1 Mesoscale Circulations

Mesoscale circulations, as explained in Chapter 1, can take a variety of shapes and sizes. Most work on the principle of unequal heating due to the albedo of the landscape. That is, the lower the albedo, the greater the magnitude of sensible heat flux over the low albedo area. Rodriguez (1992) showed how albedo and terrain variability work together to enhance the production of sensible heat fluxes. It was also shown that lowering the surface albedo by just 10 percent can cause a significant increase in the amount of vertical heat flux. When you surround an area of low albedo with an area where the albedo is higher, you set the stage for a mesoscale circulation (Segal et al., 1992). Most variations should result in relatively weak mesoscale circulations. However, when the albedo difference is large, a significant circulation can form. An example of this is the study done by Pielke et al. (1990) in southern Utah/northern Arizona. On June 7, 1986, albedo differences across the area ranged from approximately .15 to .28 (see Figure 2.1b). This resulted in a simulated vertical velocity of up to 15.1 cm s^{-1} when modeled using the CSU mesoscale model, RAMS (see Figure 2.1b). Anthes (1984) suggested that vertical velocities of 10 cm s^{-1}, when combined with low-level moist static energy, appear capable of initiating and enhancing moist convection under appropriate atmospheric conditions. The sea breeze, mountain-valley slope flow, snow breeze, heat island flow, and irrigated/dryland breeze are all examples of mesoscale circulations.

There have been several attempts to use numerical atmospheric models to demonstrate the potential effects of landscape characteristics on climate. A sea breeze case was modeled by McCumber (1980) showing the effect of vegetation on the development of the

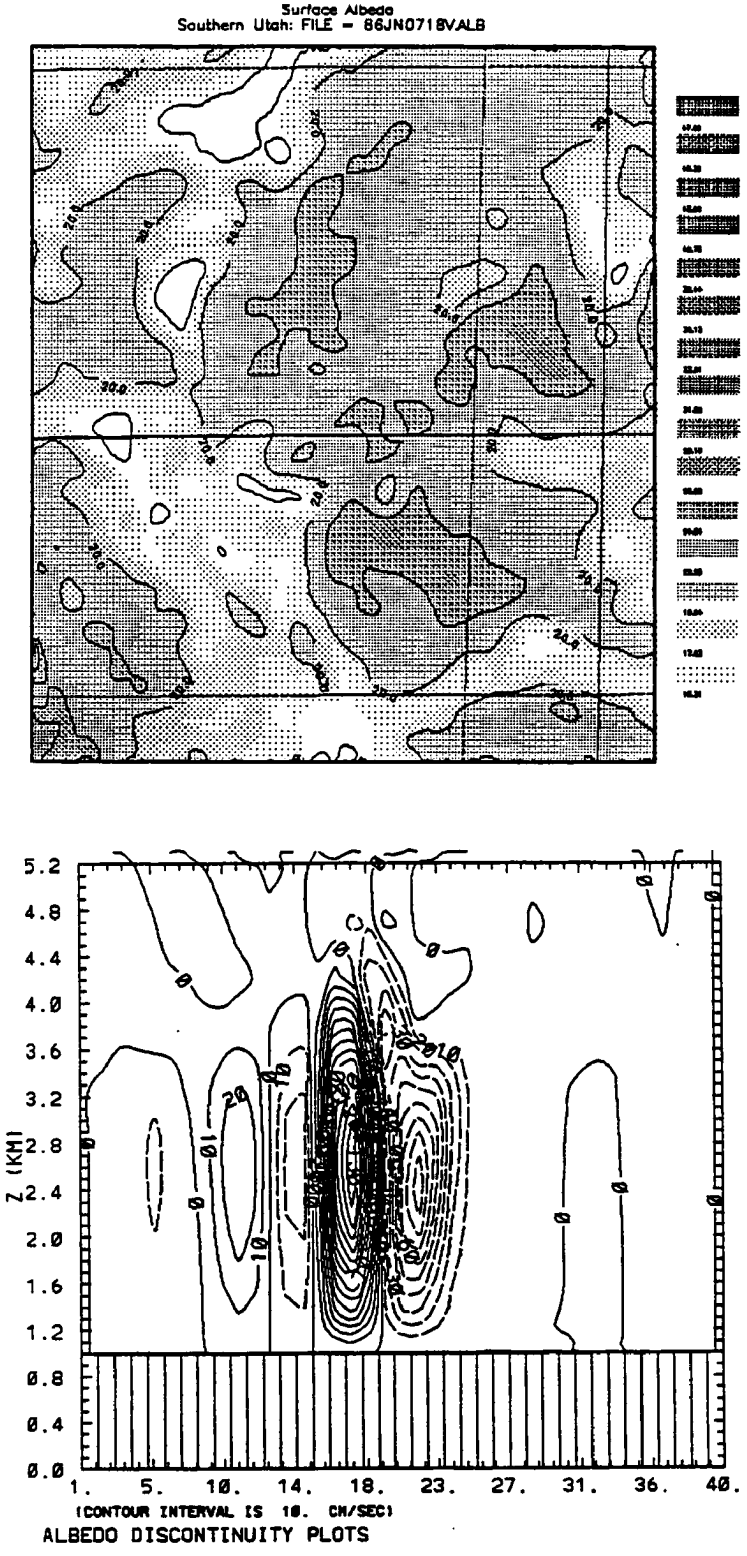

Figure 2.1: (a) Smoothed surface albedo, and (b) vertical velocity (from Pielke et al., 1990).

sea breeze. The model showed that the type of vegetation along with the percent coverage can have a significant effect on the strength of the sea breeze. A study by Anthes (1984) demonstrated that mesoscale circulations can be generated by the thermal contrast between vegetated and bare, dry areas in subtropical latitudes. Mahfouf et al. (1987) showed how locating a dry, bare land next to a transpiring vegetation can generate circulations as strong as sea breezes. Studies by Segal et al. (1988) and (1989) also suggested that for dense, well-watered and extended crop areas, mesoscale circulations of an intensity close to that of a sea breeze may result. The study by Segal et al. (1988) was supported by surface observations and infrared surface temperatures obtained from the Geostationary Operational Environmental Satellite (Pielke and Avissar, 1990). The results showed that differences in landscape characteristics in areas as small as 10 square kilometers could generate a sea breeze strength circulation. Avissar and Pielke (1991) showed how plant stomata could have a significant effect on the strength of mesoscale circulations. If the plants are under strong stress, they will not transpire, and the sensible heat flux produced over the vegetation is almost identical to that obtained over a bare surface (in this case, a fire burned area). Thus, the vegetation will not contribute significantly to the production of a mesoscale circulation.

Observational evidence that the daytime thermally-induced flow between snow cover and snow-free areas can generate a significant mesoscale circulation has also been documented. Segal et al. (1991)a and b showed that sensible heat flux characteristics over snow surfaces are much less than over an adjacent snow-free area under the same environmental conditions. The horizontal thermal gradient between the snow area and the snow-free area would become evident as the snow breeze. Possible evidence of the snow breeze includes suppression of the daytime thermally-induced upslope flow over snow covered area and possible reversal of the daytime drainage flow over the slope. During the early spring, combining the convergence associated with the snow-line retreat with the thermally-induced upslope flow may enhance convective cloud formation. A study by Johnson et al. (1984) used data from the Program for Regional Observing and Forecasting Services (PROFS) surface mesonetwork to document the effect of variable snow cover

on atmospheric boundary layer properties, cloudiness and weather conditions over northeast Colorado. The study suggested that snow boundaries in the region may have acted through the development of a weak solenoidal field to enhance low-level inflow into the snow-free area, aiding in the development of clouds in the region. The stability of the atmosphere was weak enough to produce scattered snow showers over the snow-free area, while the snow-covered areas remained mostly clear all day.

Pielke et al. (1990) utilized satellite, surface/upper air observations and modeling to evaluate mesoscale circulations forced by surface gradients of heating arising from irrigated areas adjacent to dry land. The Bowen ratio (ratio of surface sensible heat flux to that of evapotranspiration flux) is lower than that of the surrounding dry land areas. This results in a horizontal gradient of sensible heat between the two areas and generation of mesoscale circulations. Temperature contrasts of up to 10 degrees Celsius between the two areas at noon were observed, along with a significant moisture difference of up to 6 g kg^{-1}. In addition, thermally-induced flow was most pronounced for zero mean synoptic flow. In addition, a study by Pielke and Zeng (1989) found that larger available potential energy exists in the lower troposphere over irrigated land than exists over adjacent natural grassland. The study, conducted using radiosonde sounding data collected over northeast Colorado, suggests that this enhanced energy could be a mechanism for potentially enhanced thunderstorm severity over and near irrigated locations. Differential turbulent sensible heating between the two land surface types could also develop low-level convergence which, in turn, would further enhance any available buoyant energy.

Xian and Pielke (1991) used a two-dimensional hydrostatic model to simulate sea-breeze circulation response to different sized landmasses. It was shown that the landmass sizes along with differing vertical lapse rates, horizontal synoptic flow, and latitude all had an effect on sea-breeze strength. The strongest vertical motions developed using a weakly stable vertical lapse rate in light synoptic flow ($\leq$ 2.5 m s^{-1}). The study found vertical velocities approaching 1.2 m s^{-1} for landmasses up to 200 km (Figure 2.2a). Even the 24 km landmass produced a vertical velocity of 15 cm s^{-1} (Figure 2.2b).

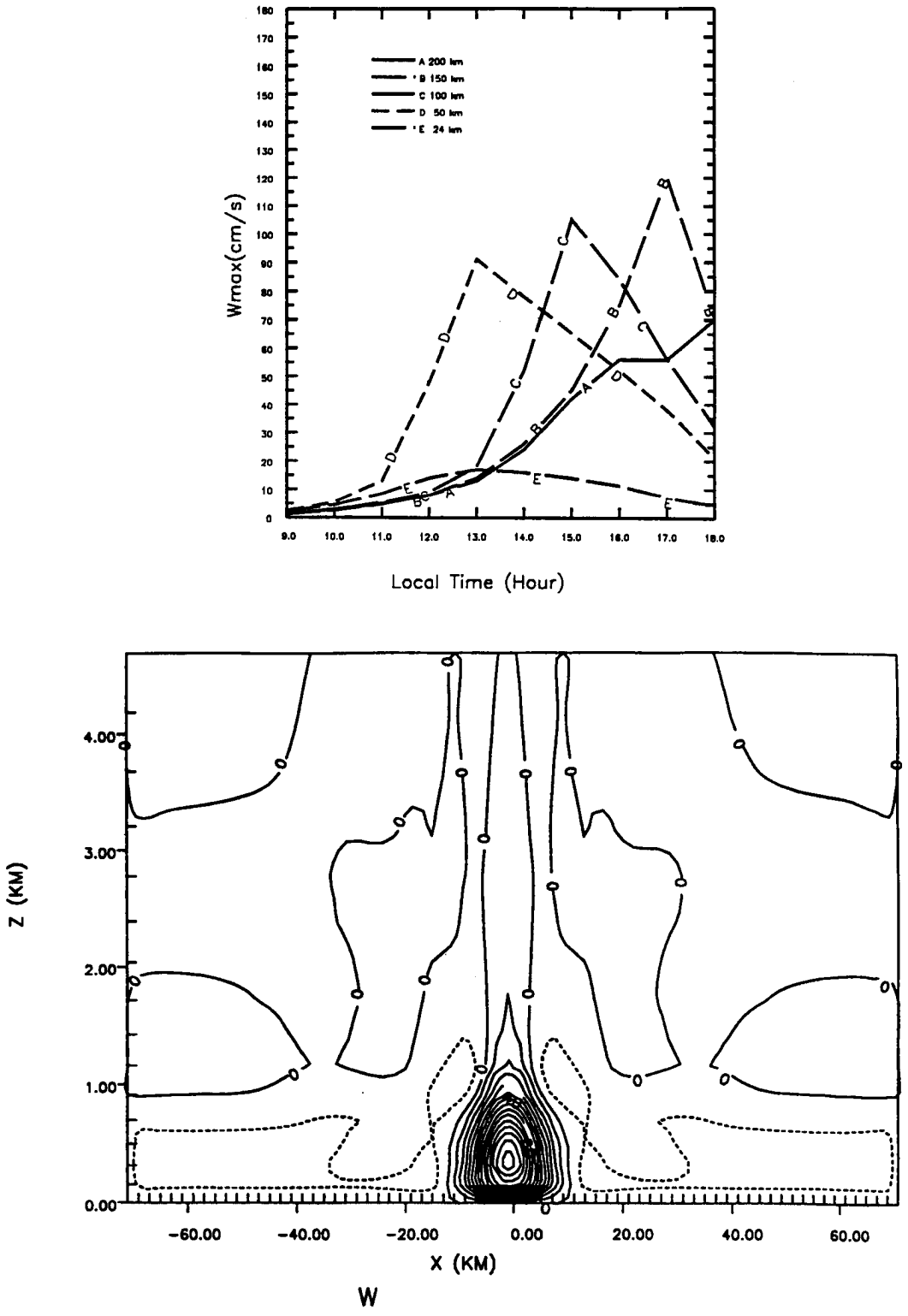

Figure 2.2: (a) Vertical velocities, and (b) 24 km vertical velocity (from Xian and Pielke, 1991).

2.2 Alaskan Forest Fires

As stated earlier, forest fires in Alaska occur frequently. They can be big or small, started by lightning or man, and last for hours or days. Lightning-caused fires are often the longer lasting of the two types, mainly because lightning-caused fires are more likely to start in remote areas (Flannigan et al., 1991). The remoteness of the fires requires the use of helicopters to transport men and equipment to the fires. Research by Fuquay et al. (1967, 1972, and 1979) has shown that the long-continuing current (LCC) phase of a lightning discharge is responsible for most, if not all, lightning-caused fires. But, not every LCC will ignite a fire and not every discharge contains a LCC phase. Most lightning detection equipment can discern this LCC phase in lightning discharges. Thus, fire management agencies can use the LCC phase detection to identify potential locations of fire starts. The study by Flannigan et al. (1991) also found that negative-charged lightning discharges ignited more fires than positive-charged lightning discharges.

Whatever the cause, forest fires have a long-term effect on the environment, as well as animals, plants, and even man. The obvious effect is the burning of vegetative matter including trees, grass, and the biomass of the forest floor (Viereck et al., 1979). The thick biomass on the forest floor is very important to the post-fire recovery of the area. In the Wickersham Dome fire (located about 50 miles northwest of Fairbanks, Alaska) of 1971, the average biomass thickness previous to the fire was 28.7 cm. Average reductions after the fire were 10.3 cm for heavily burned areas and 5.7 cm for lightly burned areas. Thus, two-thirds of the forest floor remained after the fire.

The reduction of forest floor biomass and blackening of the surface by fire causes higher soil temperatures (Viereck et al., 1979). In this case, up to a 5 degree Celsius difference was noted between the burned and unburned areas at a depth of 10 cm. The burned area also heated up much faster than the unburned area, with the maximum temperature being reached by July in the burn area compared to September in the unburned area. The main effect of the increased temperature was a stepped up rate of permafrost melting. The active layer of melting in non-burned ground is 45 cm, while the active layer on

the Wickersham Dome fire site was as deep as 132 cm by the third year. Such thawing substantially increases the amount of available soil nutrients and soil water.

Recovery of vegetation depended primarily on the severity of the fire. In the Wickersham Dome fire, a lightly burned black spruce plot (Figure 2.3a) still had 40 percent of the ground vegetative cover alive after the fire (Viereck et al., 1979). This increased to 70 percent within 3 years of the fire. In contrast, recovery of vegetation on a heavily burned black spruce plot (Figure 2.3b) was much slower. Only 15-20 percent had recovered after 3 years. Overall, about 50 percent of the vegetation recovered by the 3-year point in the Wickersham Dome burn area. The Wickersham Dome fire was considered fairly typical of the wildfires that occur in the Alaska interior. Specific areas in the burn area were totally recovered within 3 years while other areas took 5-10 years. The same rates apply to the trees. Depending on the severity of the fire, recovery of the trees is dependent on the survival of the shoots that grow from the forest floor. Shoot survival is dependent on several points, to include adequate water, soil nutrients, even consumption by the local snowshoe hare population. One other important consequence of wildfires is the possible effect on the quality of stream water. There are speculations that fires, by way of burning away all ground cover, add to increased erosion and soil runoff.

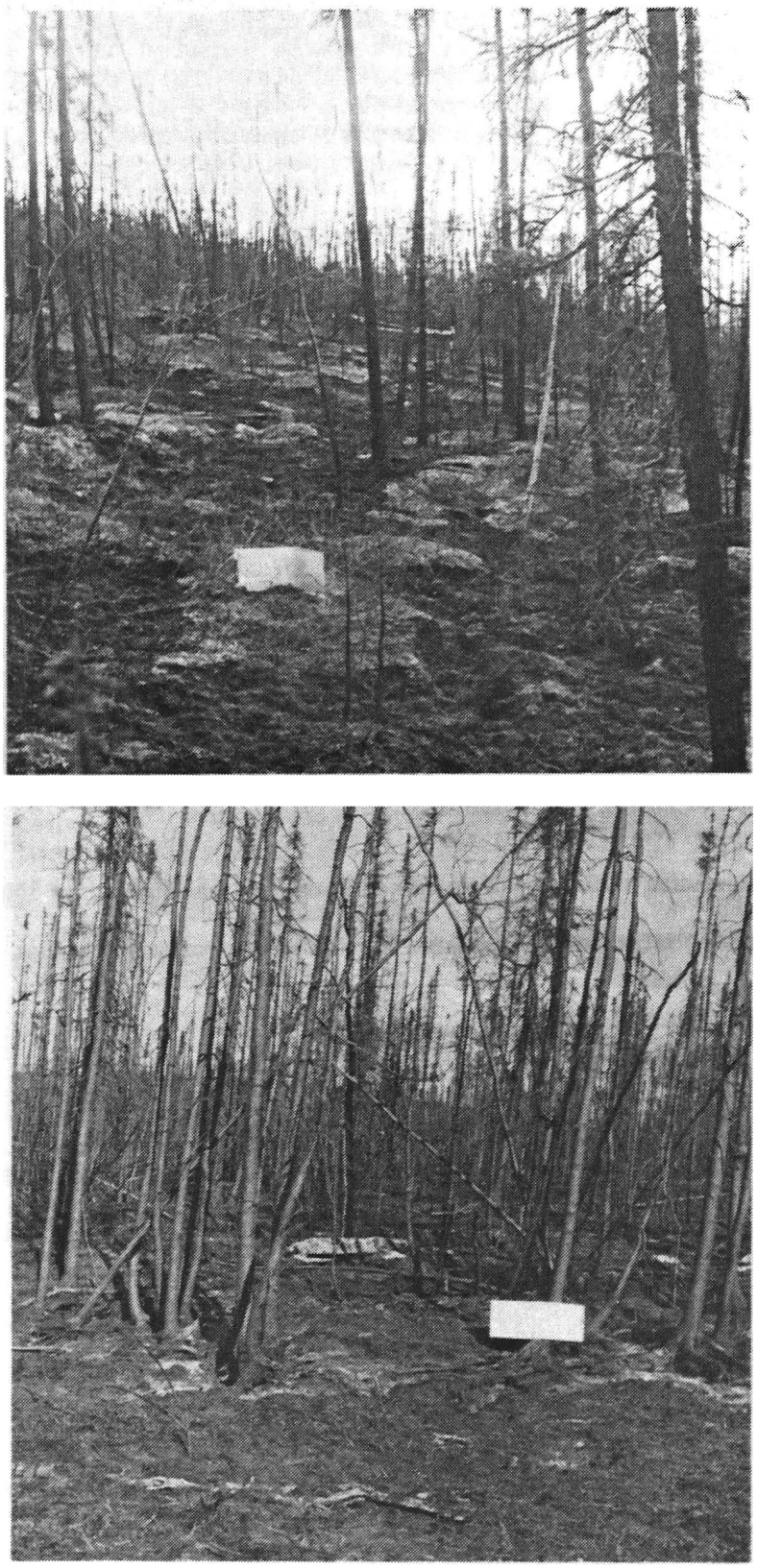

Figure 2.3: (a) Lightly burned stand, and (b) heavily burned stand (from Viereck, 1976).

Chapter 3

NUMERICAL MODEL DESCRIPTION

3.1 The Regional Atmospheric Modeling System (RAMS)

RAMS was developed for simulating and forecasting meteorological phenomena, and for depicting the results (Pielke et al., 1992). Its major components are:

- An atmospheric model which performs the simulations.
- An isentropic analysis package which prepares initial data for the atmospheric model from observed meteorological data.
- A post-processing model visualization and analysis package which interfaces atmospheric model output with a variety of visualization software utilities.

3.2 The Basic Equations

RAMS uses a full set of primitive dynamical nonhydrostatic equations which govern atmospheric motions. The variables to be predicted upon will be the three momentum components (u, v, and w), the perturbation Exner function (π') and potential temperature (Θ). Note that the equations are in tensor notation.

The Momentum Equation:

$$\frac{\partial}{\partial t}\rho_o u_i + \frac{\rho_o \Theta}{a}\frac{\partial}{\partial x_i^*}(ab^{ij}\pi') = ADV(\rho_o u_i) + \rho_o TURB(u_i) + g(\frac{\Theta'}{\Theta_o})\delta_{i3} + \epsilon_{ijk} f_3(\overline{u}_{ik} - u_{0k})$$

The Thermodynamic Equation:

$$\frac{\partial}{\partial t}\rho_o \Theta = ADV(\rho_o \Theta) + \rho_o TURB(\Theta)$$

The Continuity Equation:

and,

$$\frac{\partial}{\partial t}\pi' + \frac{1}{a}\frac{R}{C_v}\frac{\pi_o}{\rho_o\Theta_o}\frac{\partial}{\partial x_j^*}(ab^{ij}\rho_o\Theta_o u_j) = 0$$

where:

$$ADV(\rho_o A) = -\frac{1}{a}[\frac{\partial}{\partial x_k^*}(ab^{jk}\rho_o u_j A) - A\frac{\partial}{\partial x_k^*}(ab^{jk}\rho_o u_j)]$$

and,

$$a = 1 - \frac{z_s}{H} = \frac{\partial z}{\partial z^*}$$

and,

$$b^{ij} = \begin{bmatrix} 1 & 0 & \frac{1}{a}\frac{\partial z_s}{\partial x}[\frac{z^*}{H} - 1] \\ 0 & 1 & \frac{1}{a}\frac{\partial z_s}{\partial y}[\frac{z^*}{H} - 1] \\ 0 & 0 & \frac{1}{a} \end{bmatrix}$$

and,

$$z^* = H\frac{z - z_s}{H - z_s}$$

3.3 Numerical Methods

The grid structure uses the Arakawa-C grid (Mesinger and Arakawa, 1976). The advection operator is the flux form of the 2nd-order leapfrog for the horizontal advection and a forward form for the vertical advection (Tremback et al., 1987). The time split scheme (Tremback et al., 1985) is used for the model time integrations.

The minimum horizontal resolution length is 8 km and larger (with a Δx = 2 km). There are 30 levels with a minimum stretched grid of 300 m (Δz = 300 m) near the ground and up to a maximum of 600 m near the top of the model (15 km). The time step is 3 seconds. The model domain is a 40 × 40 grid points (80 km × 80 km) in the horizontal.

The lateral boundaries are chosen as Klemp and Wilhelmson (1978). The top boundary condition is a wall on top, using a modified form of Rayleigh friction (Cram, 1990) for the top 5 points.

3.4 Physical Parameterizations

As is true in all atmospheric models, several physical processes are too complicated or too time consuming to be properly calculated, and need to be parameterized. The following physical processes are parameterized by RAMS in the version used in this study:

- Cumulus Convective Scheme: Cumulus Convection is necessary to represent subgrid-scale transport by downdrafts and updrafts of cumulus clouds which vertically redistribute heat, moisture, and momentum within the model and also produce convective rainfall. The convective terms are significant forcing terms in the model. This scheme is very important in the model simulations, as the convection will give rise to lightning, a necessary ingredient if any forest fires are to be set. The convective parameterization is a modification of the Kuo (1974) scheme described by Molinari et al. (1985). The difference between the environmental potential temperature and a convective potential temperature profile is used to estimate the convective heating. Convection is activated if the grid column is convectively unstable and there is resolved upward vertical motion at the lifting condensation level. The source level air for the convection is defined as the highest θ_e air that is less than 3 km above the ground. The cloud top, however, is defined as the level above which the potential temperature of the moist adiabatic becomes less than the grid temperature.

- Radiation Scheme: The Chen and Cotton (1983) radiation parameterization scheme is used by RAMS. The scheme includes both solar and infrared radiation, and also includes the effects on radiative transfer of condensation, water vapor, ozone, and carbon dioxide.

- Microphysics Scheme: The microphysics parameterization scheme developed by Tripoli and Cotton (1982) and Flatau et al. (1989) is used by RAMS to work with resolved condensation and precipitation processes. Diagnostic values for the water species of vapor, rain, pristine ice crystals, snow, aggregates, and graupel are used in the model simulations. Each species can acquire mass through vapor condensation/deposition, self-collection, or interaction with another species (Papineau,

1992). The model predicts the mixing ratios of each species, while the distribution of a particular species is diagnosed.

- Turbulent Diffusion Scheme: RAMS uses a first order eddy viscosity type based on a local exchange coefficient that is a function of deformation and stability. Definitions of kinetic and thermal eddy coefficients developed by Xian (1991) are used in the model simulations.

- Surface Boundary Conditions: The surface layer model from Louis (1979) and soil model parameterizations of Tremback and Kessler (1985) are used. The soil model uses prognostic equations formulated from the surface energy balance for the soil surface temperature and water content by choosing a finite depth soil-atmosphere interface layer. Soil depth was taken down to 50 centimeters. This was due to the level of permafrost averaging around 40 centimeters in the summer (Viereck et al., 1979).

- Lateral Boundary Conditions: RAMS uses a radiative boundary condition with constant inflow and outflow. The scheme was developed by Klemp-Wilhelmson (1978). This permits gravity waves to propagate out of the integration domain with little apparent reflection.

3.5 Topography

The USGS 10-minute terrain data set was used for model topography (Figure 3.1). This gives a coarse representation of the terrain in Alaska, especially the higher terrain. The smoothing that takes place reduces the barrier height from 6300 meters to 3200 meters.

3.6 Model Initialization

Data used for the initial conditions was derived from the Fairbanks sounding for June 21, 1988 at 00 Z.

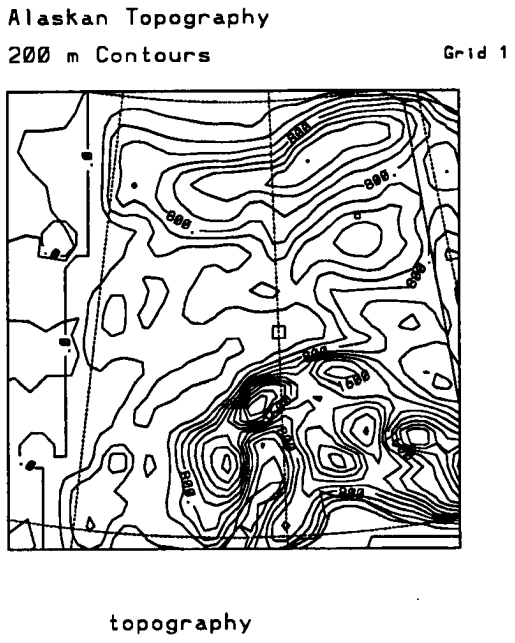

Figure 3.1: Topographical plot of the Alaskan interior, using a contour interval of 200 m MSL.

Chapter 4

CASE STUDIES

4.1 Overview

Two specific fires, each occurring during the 1988 growing season, were chosen as case studies. The specifics for each case are listed under Table 4.1 (Yarie, personal communication, 1993).

Table 4.1: Summary of Fire Data by Model Run

Model Run	Fire ID Number	Fire Start Location	Fire Size (km^2)	Fire Start Date
1	433	66.93N, 144.70W	424.92	06/15/1988
2	577	67.20N, 145.00W	148.52	07/16/1988

Both fires are located to the north of Fort Yukon. Figure 4.1 has the location of each fire on a map of the local area. Each model run utilizes the model specifics listed in Chapter 3, and is initialized using the Fairbanks 00Z 21 June 1991 RAOB sounding. See Table 4.2 for a summary of model parameters used.

4.2 Case Study 1

Model Run 1 concentrates on a large fire that broke out on 06/15/1988 due to a lightning strike. This simulation uses one grid, with 40, 40, and 30 grid points in the x, y, and z directions. The center of the simulation is the fire start location. Model run time was 8 hours, commencing at 0800 LST. Figures 4.2, 4.3, 4.4, and 4.5 show the upward vertical velocity (w) cross section in c ms^{-1} at a point running east-west 1 km south of the fire center. Plot times are 1000, 1200, 1400, and 1600 LST.

Table 4.2: Summary of Model Parameters Used

Primitive Equations	Nonhydrostatic
Grid Points	40, 40, 30 in x, y, z
Grid Spacing	2 km in x, y and variable in z ranging from 10 to 15000 m
Timestep	3 seconds
Radiation	Chen-Cotton parameterization, updated every 300 seconds
Top Boundary	Wall on top
Albedo	0.15, with 0.05 in burn area
Surface Roughness	0.05 m
Soil Parameterization	Tremback and Kessler, 8 soil levels
Microphysics	Explicit
Initialization	Horizontally Homogeneous using Fairbanks, Ak Sounding
Diffusion	Deformation

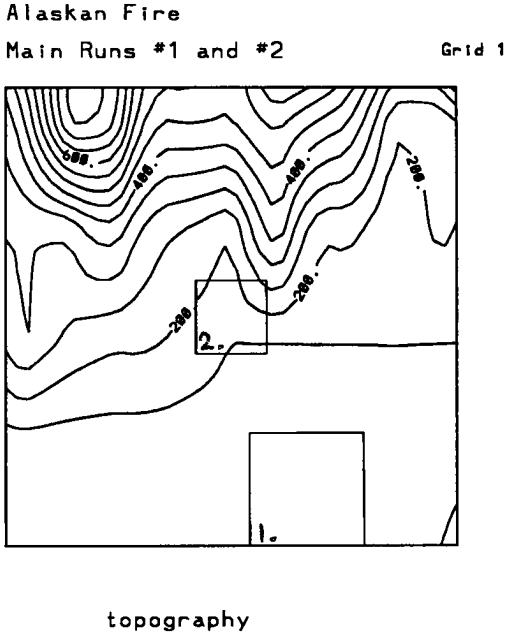

Figure 4.1: Topographical location of Runs 1 and 2, using a contour interval of 50 m MSL.

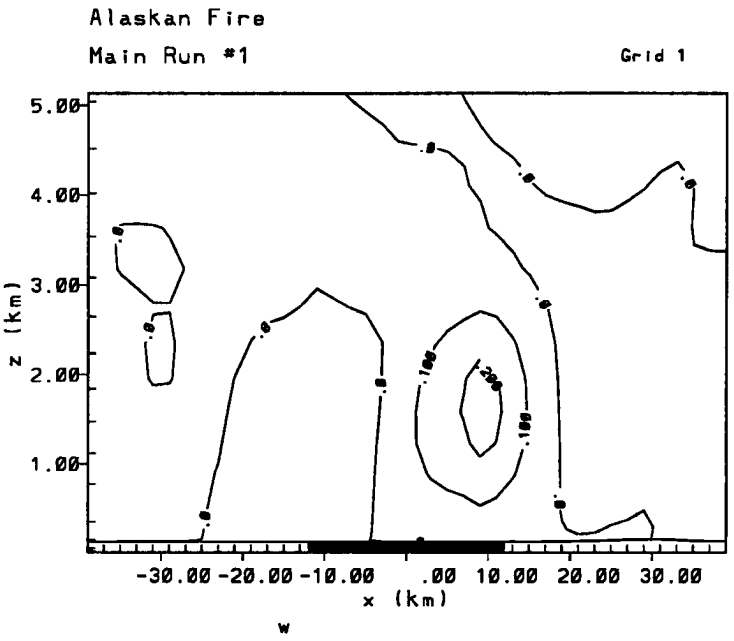

Figure 4.2: Vertical velocity field (w) in cm s^{-1} of Run 1 at 1000 LST, using a contour interval of 10 cm s^{-1}.

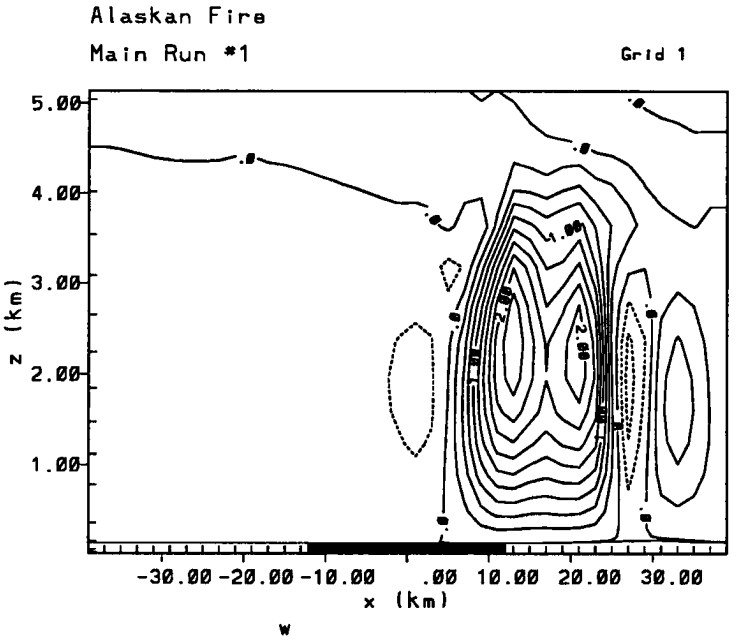

Figure 4.3: Vertical velocity field (w) in cm s^{-1} of Run 1 at 1200 LST, using a contour interval of 10 cm s^{-1}.

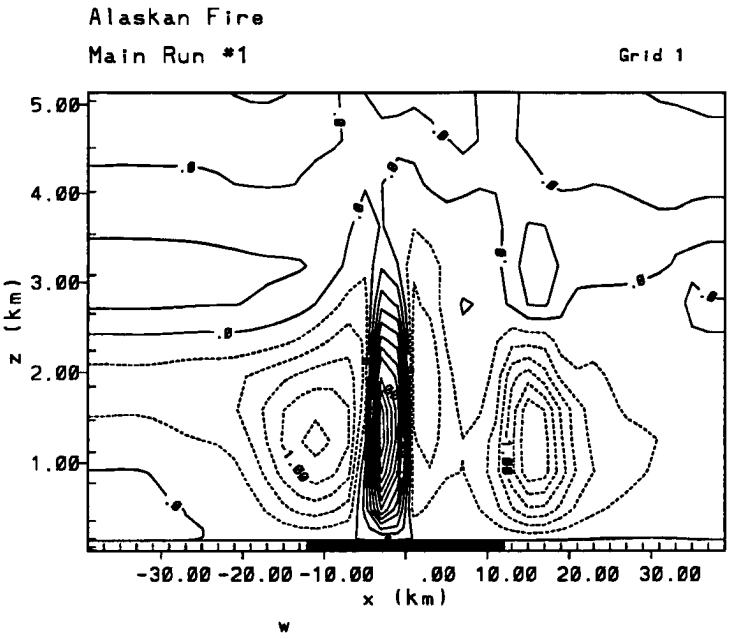

Figure 4.4: Vertical velocity field (w) in cm s^{-1} of Run 1 at 1400 LST, using a contour interval of 10 cm s^{-1}.

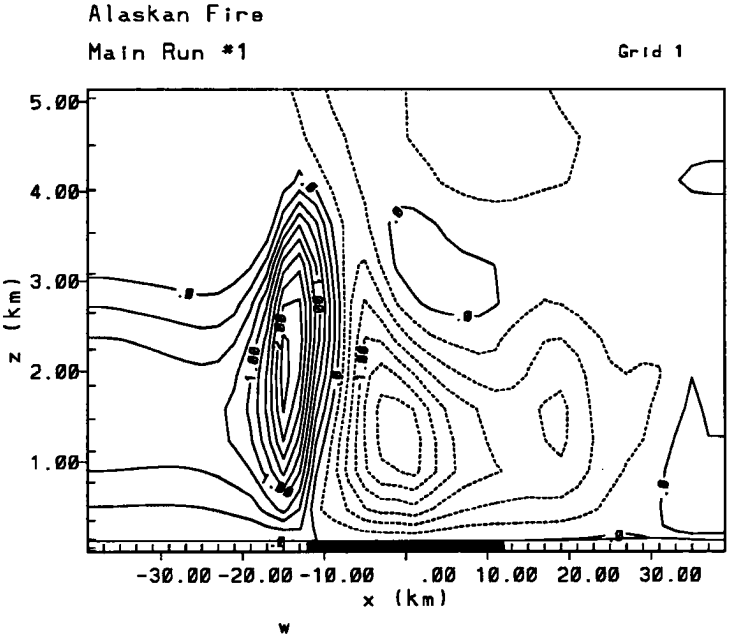

Figure 4.5: Vertical velocity field (w) in cm s^{-1} of Run 1 at 1600 LST, using a contour interval of 10 cm s^{-1}.

The first circulation center begins to develop by 1000 LST and by 1200 LST has moved almost 20 km to the east of the burn center and attained a maximum upward velocity of 2.25 m s^{-1}. The circulation center moves off to the east and dissipates over the next hour. A new circulation center develops over the center of the burn area and attains maximum upward velocity strength by 1400 LST. This center slowly weakens over the next 2 hours and moves 12 km to the east of burn center by 1600 LST.

Figures 4.6, 4.7, 4.8, and 4.9 show the upward vertical velocity field at approximately 1.8 km AGL in cm s^{-1} over the entire $x - y$ domain of the simulation. Plot times are at 1000, 1200, 1400, and 1600 LST.

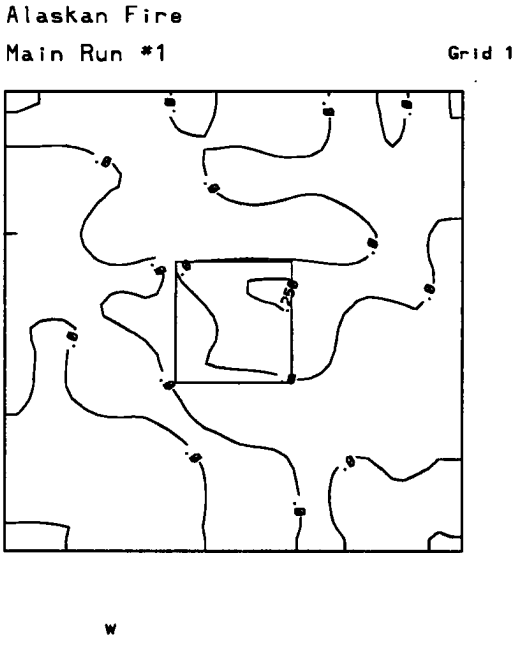

Figure 4.6: Vertical velocity field (w) in cm s^{-1} of Run 1 at 1000 LST at 1.8 km AGL, using a contour interval of 10 cm s^{-1}.

We again see the pattern that developed in Figures 4.2–4.5. A strong updraft develops just to the east of the burn area and dissipates over the next 2 hours. A large area of downward vertical velocities develops by 1300 LST, and begins to expand outward in all directions. This continues through 1600 LST with a narrow band of convergence being generated between the downdraft and updraft areas.

Figures 4.10, 4.11, 4.12, and 4.13 illustrate the horizontal wind flow associated with the circulations at 1000, 1200, 1400, and 1600 LST.

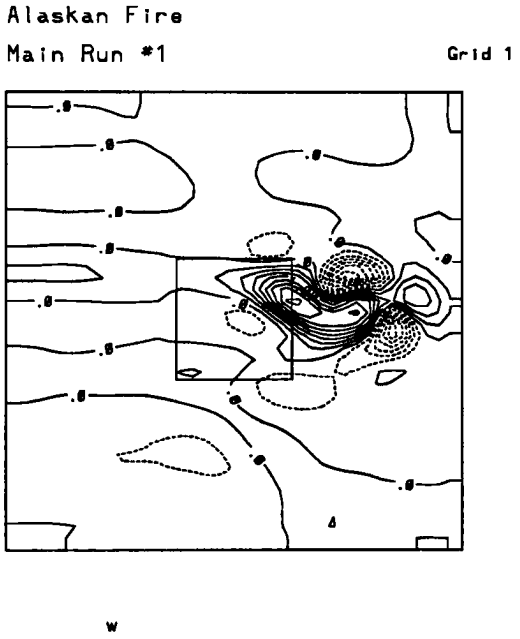

Figure 4.7: Vertical velocity field (w) in cm s^{-1} of Run 1 at 1200 LST at 1.8 km AGL, using a contour interval of 10 cm s^{-1}.

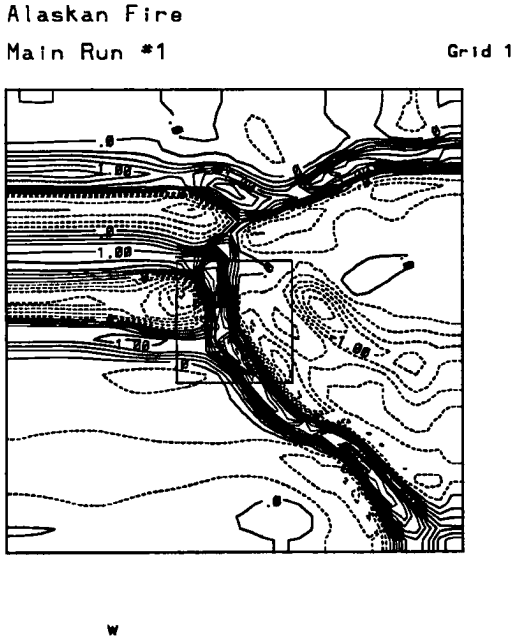

Figure 4.8: Vertical velocity field (w) in cm s^{-1} of Run 1 at 1400 LST at 1.8 km AGL, using a contour interval of 10 cm s^{-1}.

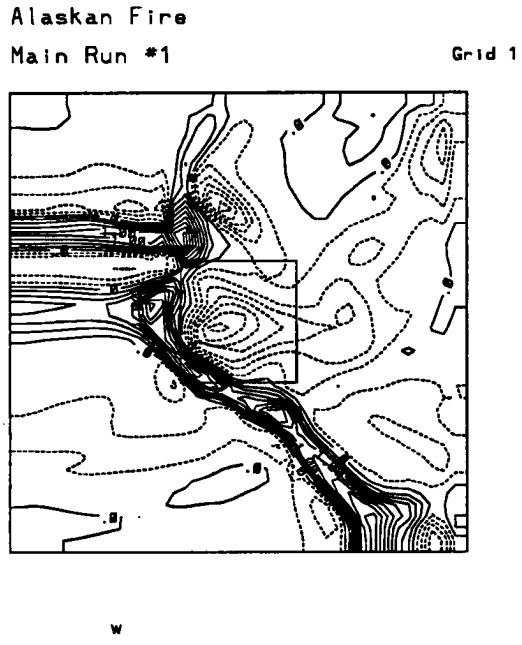

Figure 4.9: Vertical velocity field (w) in cm s^{-1} of Run 1 at 1600 LST at 1.8 km AGL, using a contour interval of 10 cm s^{-1}.

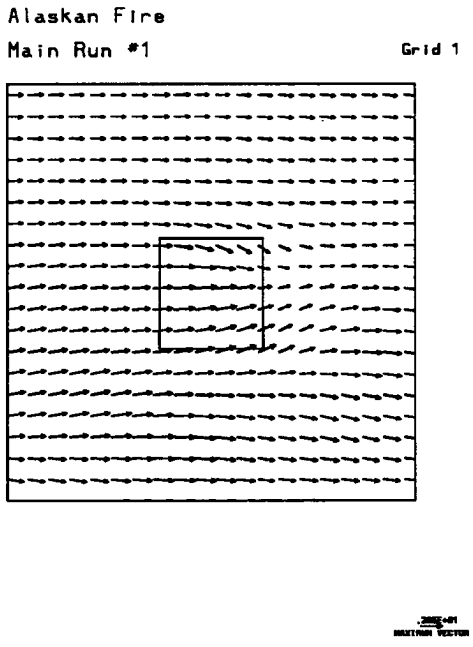

Figure 4.10: Horizontal wind vectors in m s^{-1} of Run 1 at 1000 LST at 16.8 m AGL.

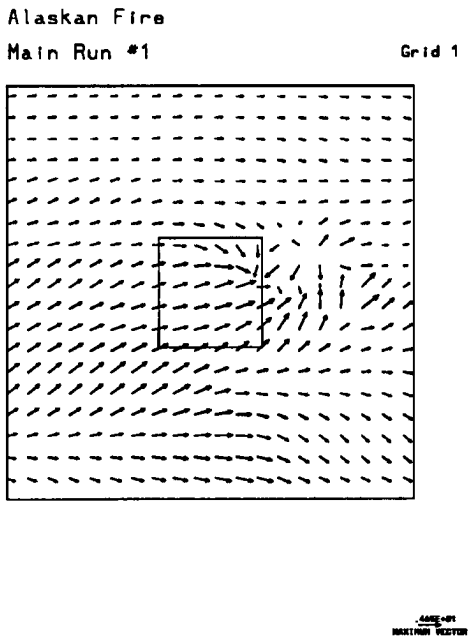

Figure 4.11: Horizontal wind vectors in m s^{-1} of Run 1 at 1200 LST at 16.8 m AGL.

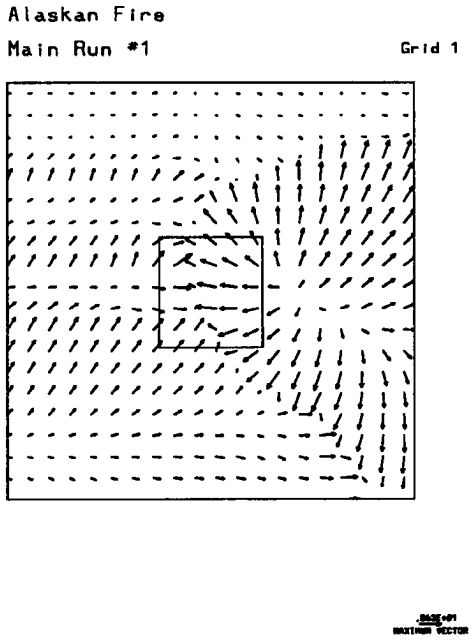

Figure 4.12: Horizontal wind vectors in m s^{-1} of Run 1 at 1400 LST at 16.8 m AGL.

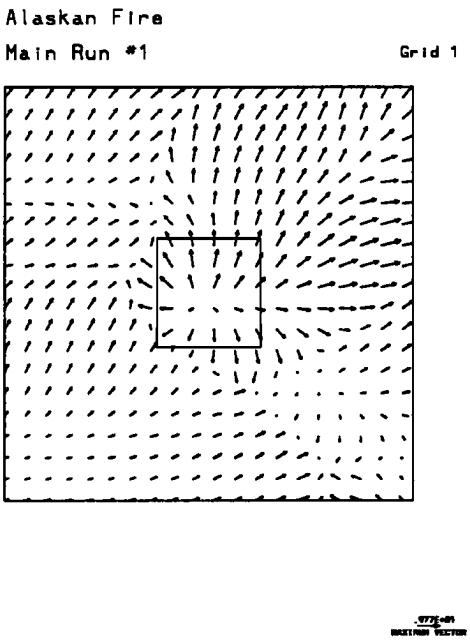

Figure 4.13: Horizontal wind vectors in m s^{-1} of Run 1 at 1600 LST at 16.8 m AGL.

The circulation center does not make its appearance until 1000 LST and slowly strengthens through 1100 LST. Strong convergence can be observed downwind of the burn area at 1100 LST. By 1300 LST, a strong downdraft can be observed off to the east of burn area. The downdraft expands through 1400 LST. The flow pattern begins to break down after that and slowly weakens over the next 2 hours, although weak convergence and divergence areas continue to form and dissipate through 1600 LST.

Figures 4.14, 4.15, 4.16, and 4.17 show the thermal structure of the circulation centers at 1000, 1200, 1400, and 1600 LST.

The plots show how the temperature field reacts to the solar heating. The fields show the effects of the upward and downward vertical velocities. Strong warming is associated with the updraft areas and strong cooling is associated with the downdraft areas. The temperature fields are slow to rise, starting from a minimum of 17.2°C at 0800 LST, and reaching a maximum of 20.2°C at 1500 LST. A possible reason for this are the effects of the downdrafts plus the cloudiness.

Figures 4.18, 4.19, 4.20, and 4.21 show the development of cloud liquid water at 1100, 1200, 1300, and 1400 LST.

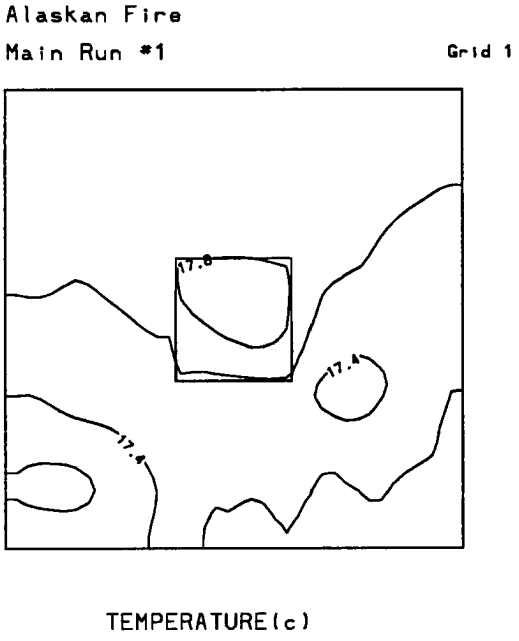

Figure 4.14: Temperature field (°C) of Run 1 at 1000 LST at 16.8 m AGL, using a contour interval of 0.2°C.

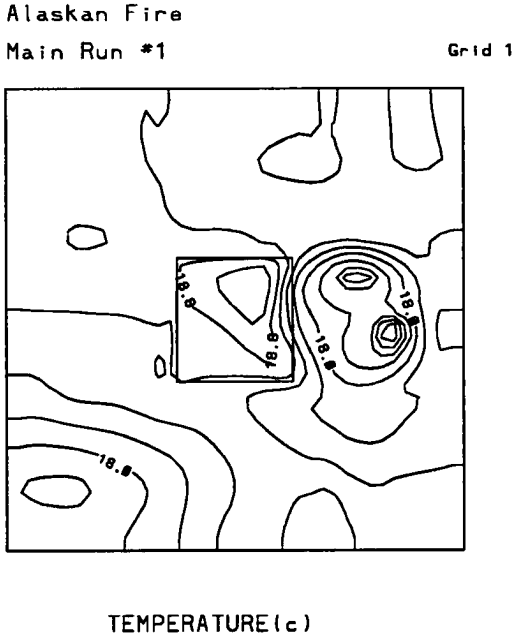

Figure 4.15: Temperature field (°C) of Run 1 at 1200 LST at 16.8 m AGL, using a contour interval of 0.2°C.

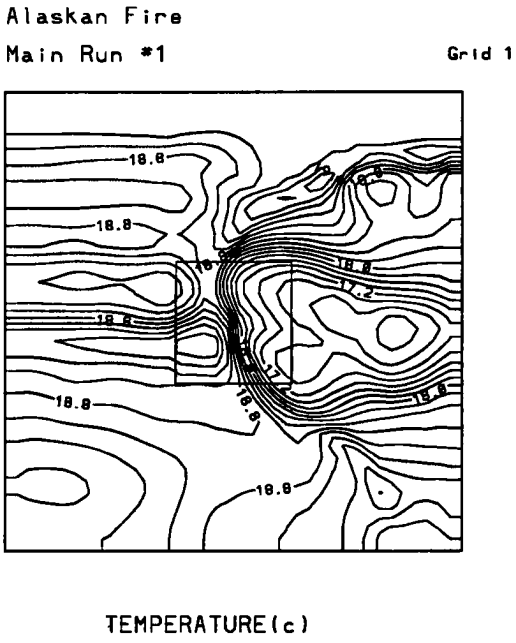

Figure 4.16: Temperature field (°C) of Run 1 at 1400 LST at 16.8 m AGL, using a contour interval of 0.2°C.

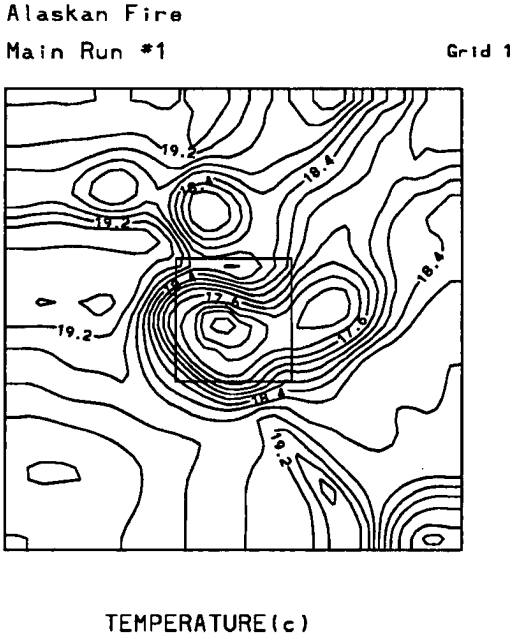

Figure 4.17: Temperature field (°C) of Run 1 at 1600 LST at 16.8 m AGL, using a contour interval of 0.2°C.

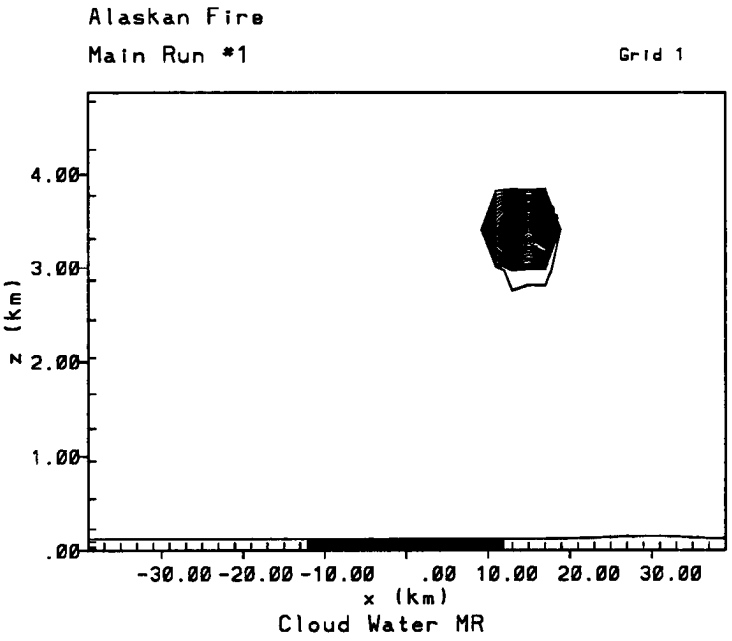

Figure 4.18: Cloud liquid water content (g kg^{-1}) of Run 1 at 1100 LST, using a contour interval of 0.02 g kg^{-1}.

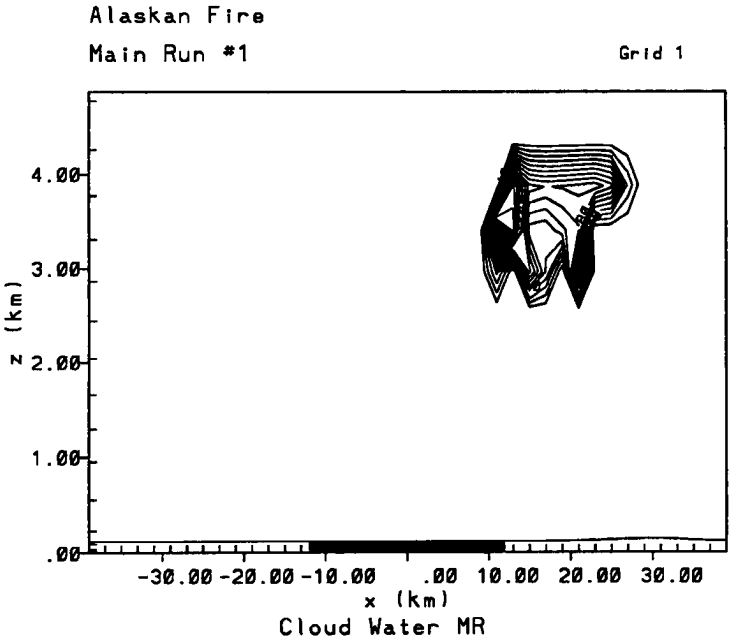

Figure 4.19: Cloud liquid water content (g kg^{-1}) of Run 1 at 1200 LST, using a contour interval of 0.01 g kg^{-1}.

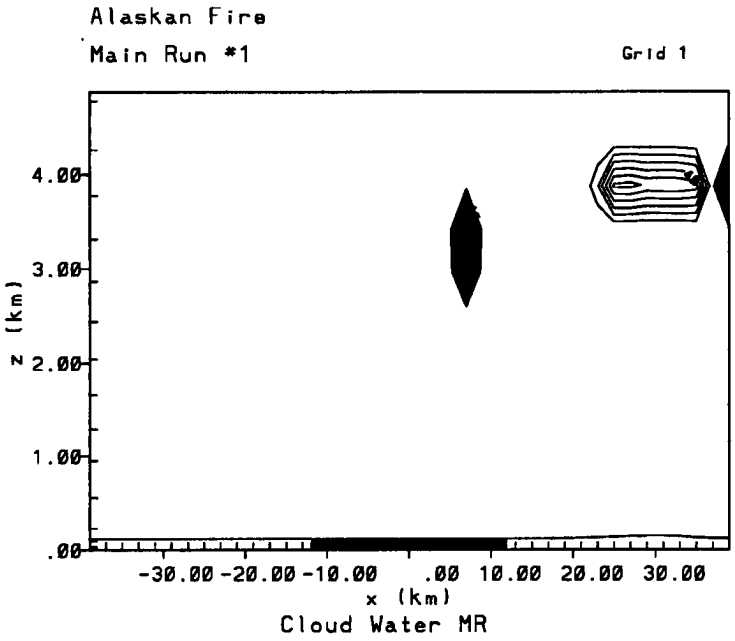

Figure 4.20: Cloud liquid water content (g kg^{-1}) of Run 1 at 1300 LST, using a contour interval of 0.01 g kg^{-1}.

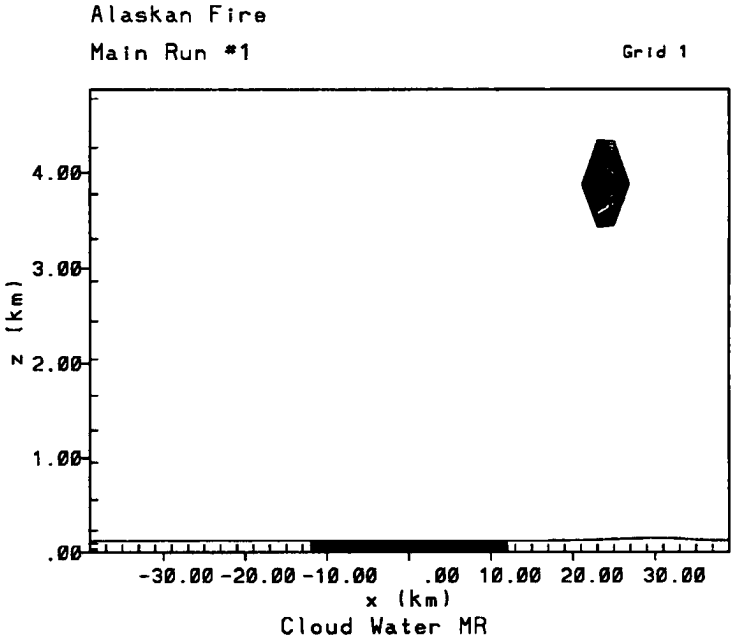

Figure 4.21: Cloud liquid water content (g kg^{-1}) of Run 1 at 1400 LST, using a contour interval of 0.002 g kg^{-1}.

A visible cloud develops by 1100 LST, and is a couple thousand meters in height. Over the next 2 hours, the cloud expands in width and height and moves off to the east out of the model domain by 1300 LST. A new cloud develops over the burn area by 1400 LST, but not to the extent of the first cloud, and is not associated with the burn area. It slowly drifts to the east through 1600 LST. The reason for the development of two separate cloud areas is the development of two circulation centers. The first cloud develops with the initial circulation center near 1100 LST. As the circulation center propagates east of the burn area, the cloud moves along with it. When the cloud gets far enough to the east of the burn area, the sun can again heat up the burn area and allow a second circulation center to develop. This second circulation center develops the second cloud area. However, it is late enough in the afternoon (1500-1600 LST) so that the solar heating is not enough to develop the circulation to the extent of the first center, therefore the cloud does not develop as much as the first. The actual visible clouds that develop during the run are larger than those visible on the cloud liquid water plots. The clouds are also consistent with the dimensions suggested by Baughman (1977). Very little precipitation fell from the clouds. Figure 4.22 shows that up to 0.70 mm was predicted by the model. Most of the precipitation fell just to east of the burn area.

4.3 Case Study 2

Model Run 2 concentrates on a fire that broke out on 07/16/1988 due to a lightning strike. This simulation uses the same set-up as Run 1 (See Table 4.2 for the model setup). Figures 4.23, 4.24, 4.25, and 4.26 show the upward vertical velocity (w) cross section in cm s^{-1} at a point running east-west 1 km south of the fire center. Plot times are 1000, 1200, 1400, and 1600 LST.

The first circulation center begins to develop by 0900 LST and by 1300 LST is located approximately 20 km to the east of burn center, and has attained an upward vertical velocity of 1.10 m s^{-1}. A second circulation has formed at this time over the center of the burn area and attained an upward vertical velocity of 0.40 m s^{-1}. The first circulation center attains an upward vertical velocity of 2.20 m s^{-1} by 1400 LST, while the second

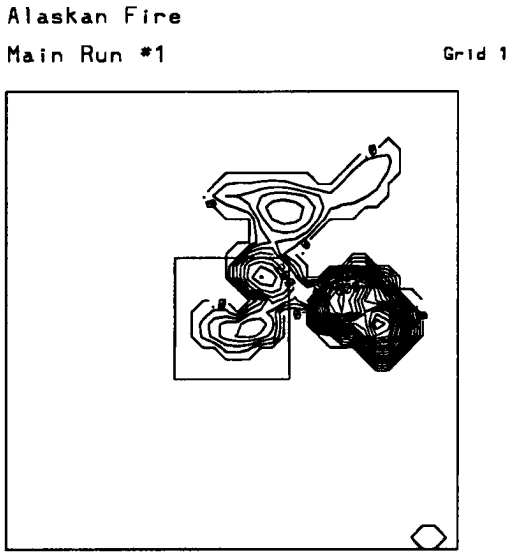

Figure 4.22: Total accumulated rainfall in Run 1 by 1600 LST, using a contour interval of 0.001 mm

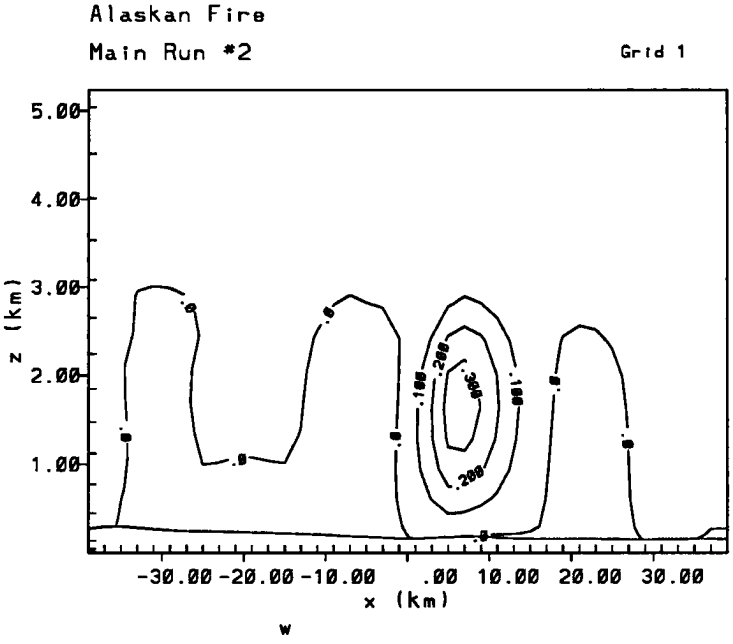

Figure 4.23: Vertical velocity field (w) in cm s^{-1} of Run 2 at 1000 LST, using a contour interval of 10 cm s^{-1}.

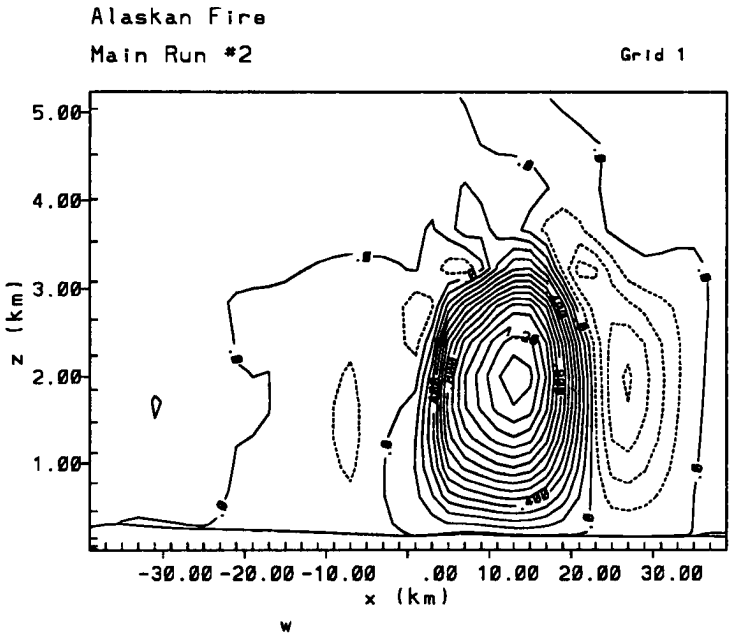

Figure 4.24: Vertical velocity field (w) in cm s^{-1} of Run 2 at 1200 LST, using a contour interval of 10 cm s^{-1}.

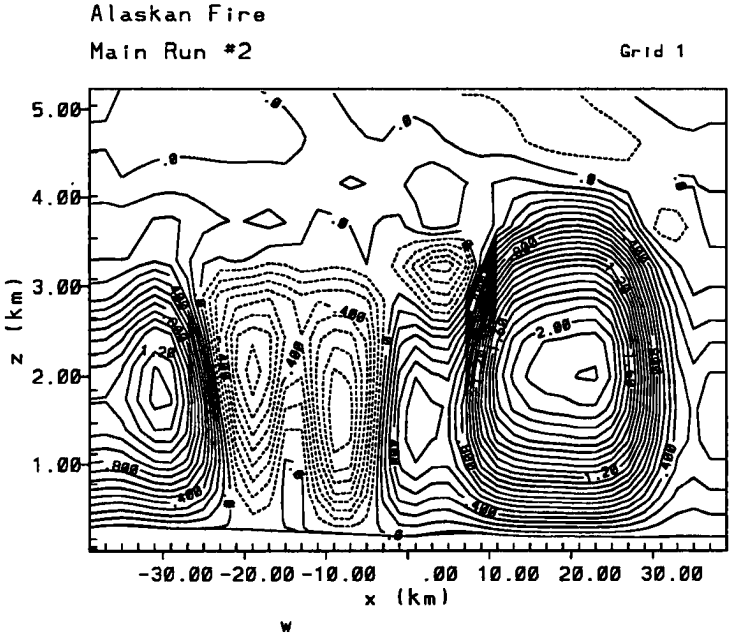

Figure 4.25: Vertical velocity field (w) in cm s^{-1} of Run 2 at 1400 LST, using a contour interval of 10 cm s^{-1}.

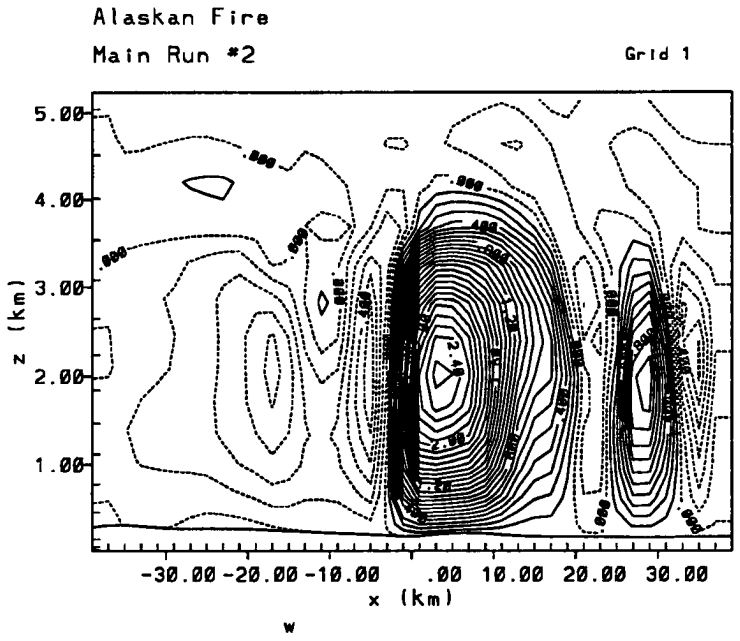

Figure 4.26: Vertical velocity field (w) in cm s^{-1} of Run 2 at 1600 LST, using a contour interval of 10 cm s^{-1}.

center does not change its strength. A third circulation center has also formed by 1400 LST in a convergence zone west of the burn area. By 1600 LST, the first center has weakened considerably, the second center has attained its maximum upward vertical velocity of 2.5 m s^{-1}, while the third center has dissipated.

Figures 4.27, 4.28, 4.29, and 4.30 show the upward vertical velocity field at approximately 1.8 km AGL in cm s^{-1} over the entire $x - y$ domain of the simulation. Plot times are at 1000, 1200, 1400, and 1600 LST.

A strong circulation cell can be seen off to the east of the burn area by 1200 LST. By 1400 LST, the pattern has become very complex as the upslope flow caused by the heating of the surrounding high terrain becomes evident in the plots. This pattern continues through 1600 LST.

Figures 4.31, 4.32, 4.33, and 4.34 illustrate the horizontal flow associated with the circulations at 1000, 1200, 1400, and 1600 LST.

The circulation center does not make its appearance until 1000 LST and slowly strengthens through 1200 LST. With the development of the second and third circulation centers, the plots become very complex. No specific circulation pattern can be found

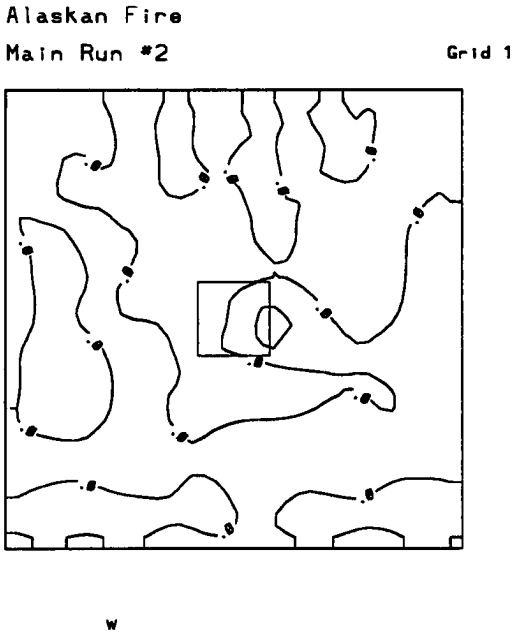

Figure 4.27: Vertical velocity field (w) in cm s^{-1} of Run 2 at 1000 LST at 1.8 km AGL, using a contour interval of 10 cm s^{-1}.

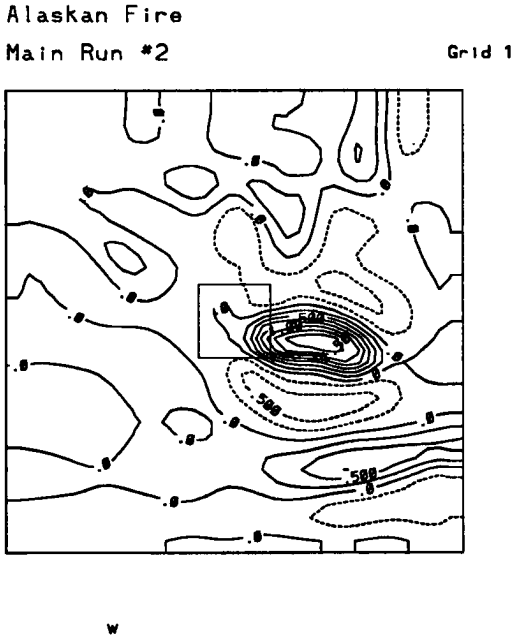

Figure 4.28: Vertical velocity field (w) in cm s^{-1} of Run 2 at 1200 LST at 1.8 km AGL, using a contour interval of 10 cm s^{-1}.

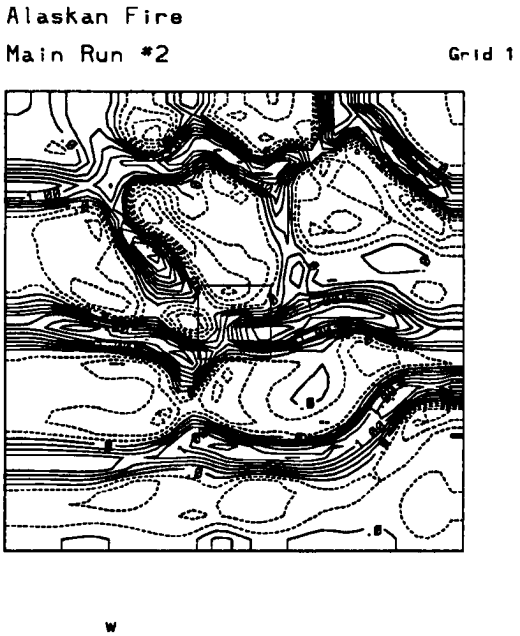

Figure 4.29: Vertical velocity field (w) in cm s^{-1} of Run 2 at 1400 LST at 1.8 km AGL, using a contour interval of 10 cm s^{-1}.

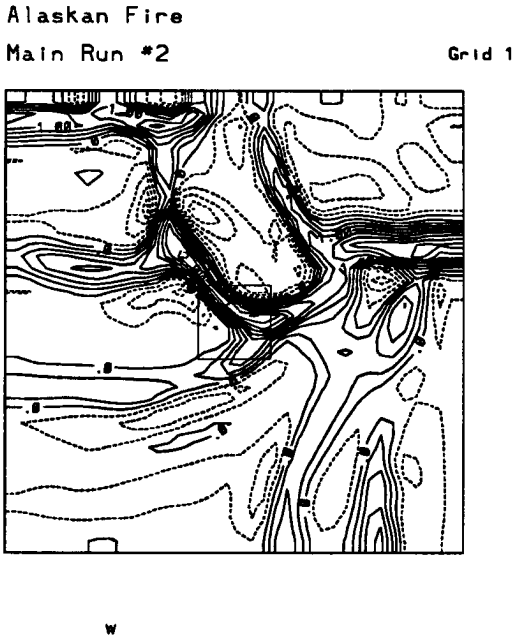

Figure 4.30: Vertical velocity field (w) in cm s^{-1} of Run 2 at 1600 LST at 1.8 km AGL, using a contour interval of 10 cm s^{-1}.

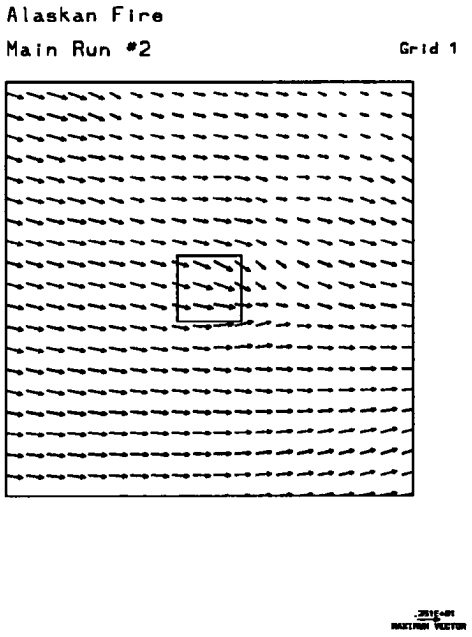

Figure 4.31: Horizontal wind vectors in m s^{-1} of Run 2 at 1000 LST at 16.8 m AGL.

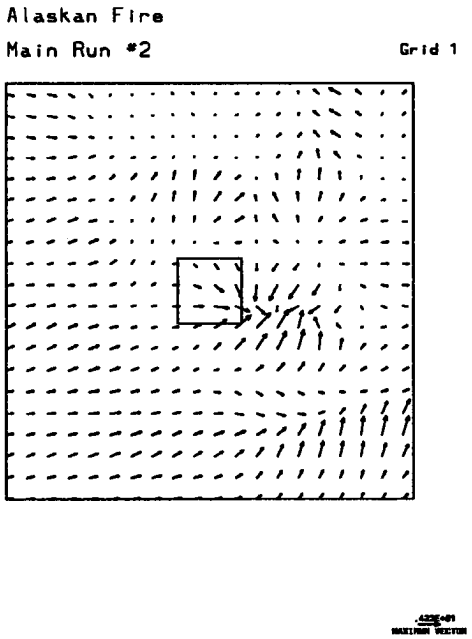

Figure 4.32: Horizontal wind vectors in m s^{-1} of Run 2 at 1200 LST at 16.8 m AGL.

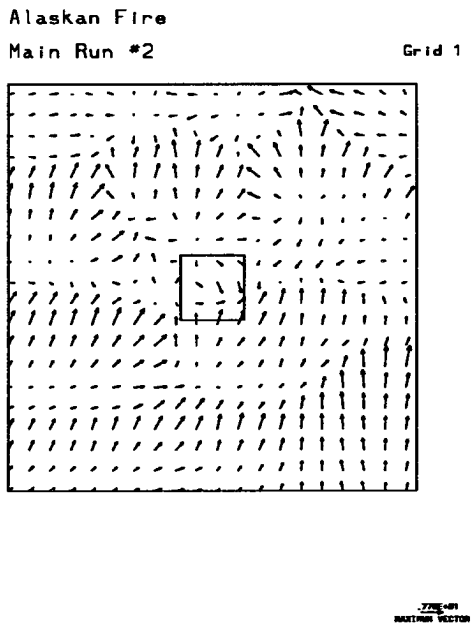

Figure 4.33: Horizontal wind vectors in m s^{-1} of Run 2 at 1400 LST at 16.8 m AGL.

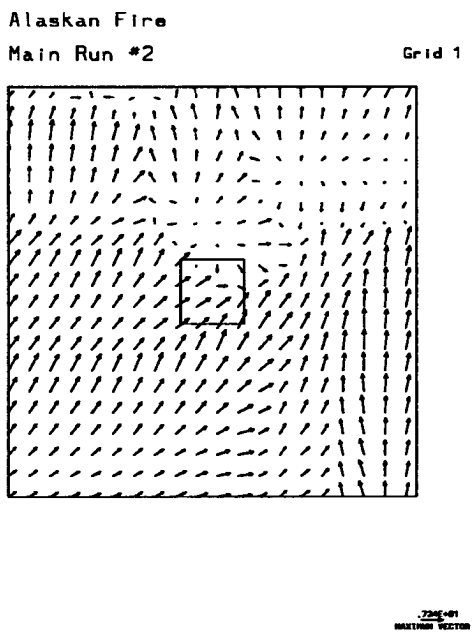

Figure 4.34: Horizontal wind vectors in m s^{-1} of Run 2 at 1600 LST at 16.8 m AGL.

from 1300 LST through 1600 LST. The effects of heating on the higher topography is clearly evident in the afternoon plots. A possible reason for the weaker circulation centers is the upslope flow to the north of the burn area.

Figures 4.35, 4.36, 4.37, and 4.38 show the thermal structure of the circulation centers at 1000, 1200, 1400, and 1600 LST.

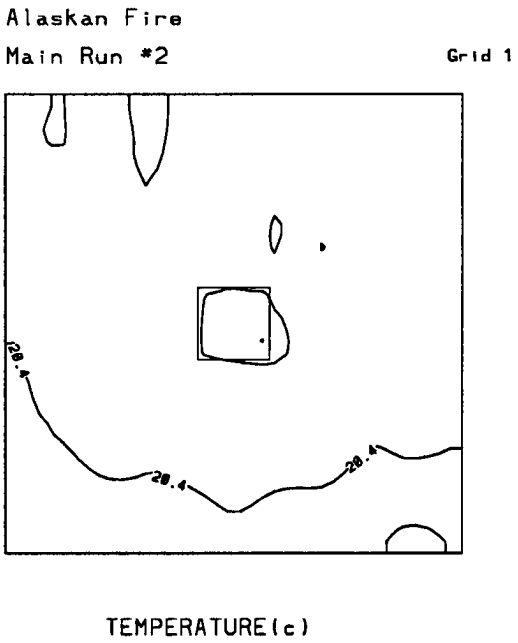

Figure 4.35: Temperature field (°C) of Run 2 at 1000 LST at 16.8 m AGL, using a contour interval of 0.2°C.

The plots again show how the temperature field reacts to the solar heating. The second run is much warmer than the first run. This may be due in part to there being no cloud development in the second run. There is nothing to block the sun. Temperatures range from 17.2°C at 0800 LST to 35.8°C at 1600 LST. The 18.6°C temperature range may seem large, but actually falls within the climatology of the Fort Yukon area (Climeo, 1979). The average temperature range during June/July is 14.36°C, and the extreme maximum temperature is 37.8°C. Given the addition of the lower albedo area acting like a heat patch, the temperatures achieved appear reasonable.

Run 2 did not develop any visible cloud liquid water. This is curious, as the updraft speeds in Run 2 (2.60 m s^{-1}) are fairly comparable to the updraft speeds in Run 1 (3.75 m s^{-1}). A possible reason for this is the complex wind motion in the area where a cloud

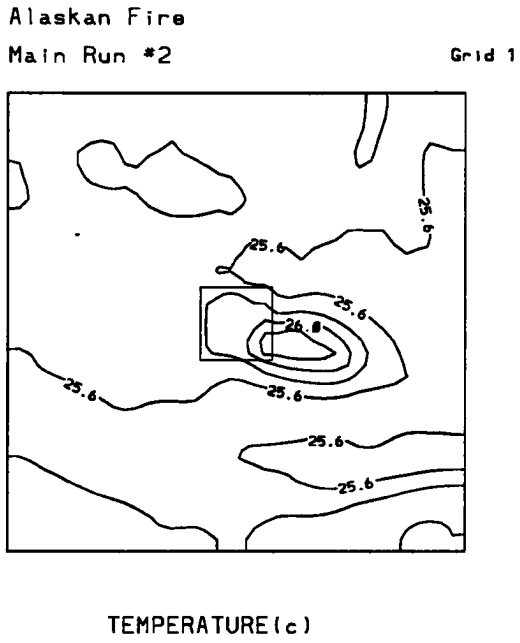

Figure 4.36: Temperature field (°C) of Run 2 at 1200 LST at 16.8 m AGL, using a contour interval of 0.2°C.

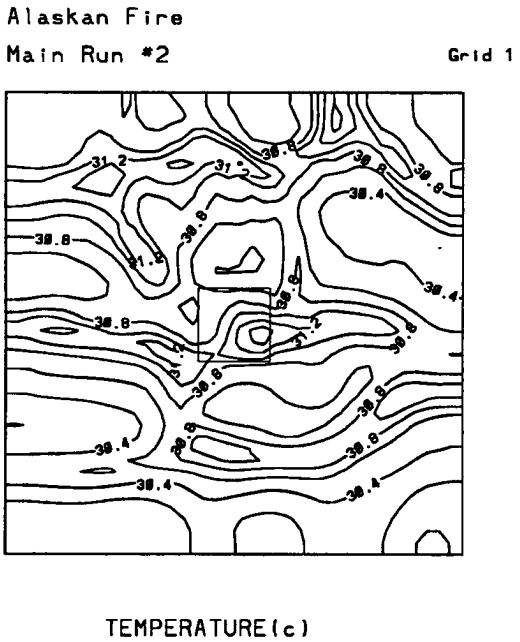

Figure 4.37: Temperature field (°C) of Run 2 at 1400 LST at 16.8 m AGL, using a contour interval of 0.2°C.

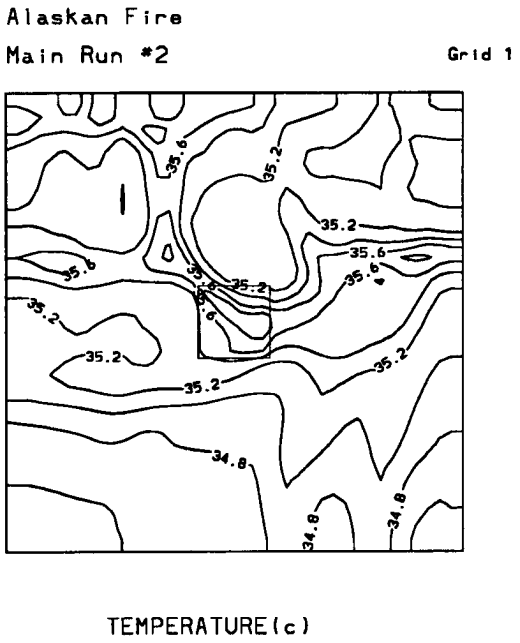

Figure 4.38: Temperature field (°C) of Run 2 at 1600 LST at 16.8 m AGL, using a contour interval of 0.2°C.

would be expected to develop. There is very little upward motion above 3 km. Another reason is that the updraft speed in Run 2 is just not strong enough to generate a cloud. Also, the upslope flow that develops over the higher terrain to the north may be having an effect on the development of circulation centers over the burn area.

4.4 Burn Area and Non-Burn Area Comparisons

Model simulations using the modification of the surface albedo corresponding to a burn area were compared to simulations having no modification of the surface albedo. All other model parameters were the same for both types of runs. Variables compared were the vertical velocity fields across the burn area at the time of maximum vertical velocity in the circulation center and the near surface temperature fields at 1200 LST. Also examined were the values of sensible heat flux (W m^2) at the surface. This was to show what effect the burn area had on sensible heat values. Figures 4.39 and 4.40 show the vertical velocity fields across the burn area for Run 1 (burn area) and Run 1a (non-burn area) at 1200 LST. Figures 4.41 and 4.42 show the near surface thermal structure of Runs 1 and 1a at 1200 LST. In the simulations without the burns, the diurnal heating of the irregular terrain in the region is the mechanism which can produce mesoscale circulations.

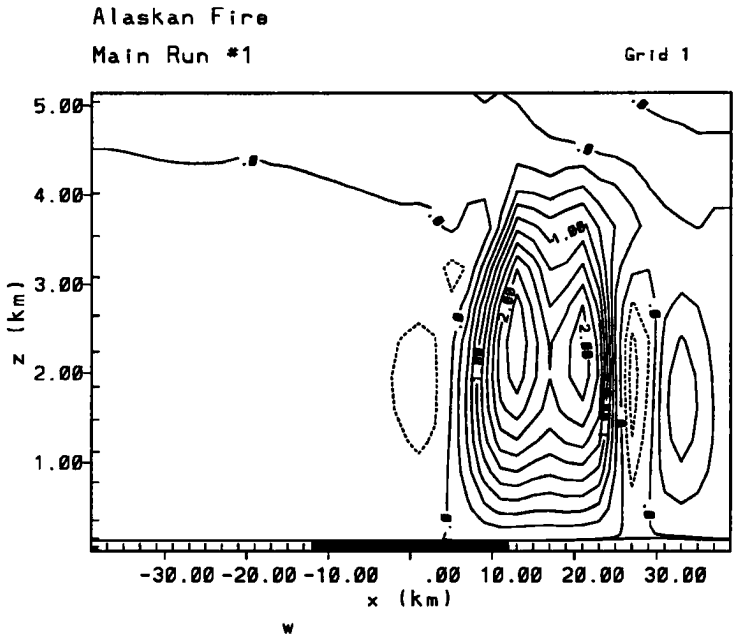

Figure 4.39: Vertical velocity field (w) in cm s^{-1} of Run 1 at 1200 LST, using a contour interval of 10 cm s^{-1}.

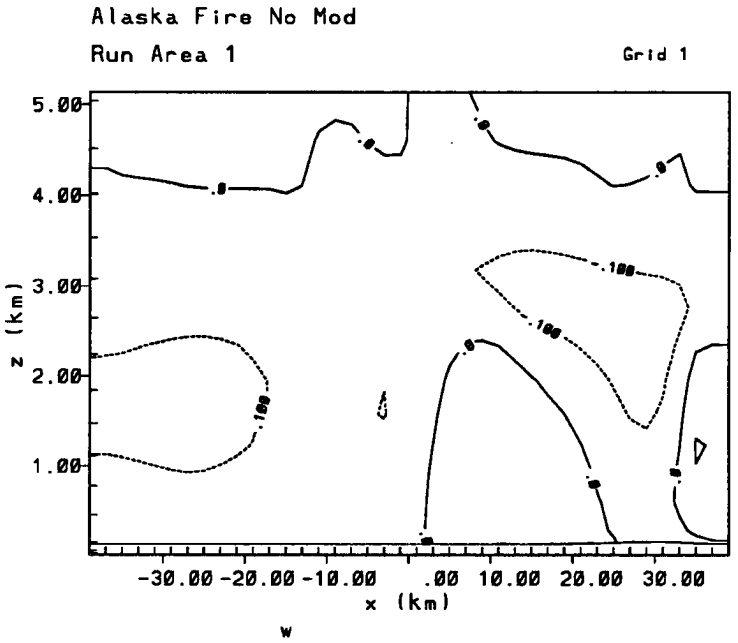

Figure 4.40: Vertical velocity field (w) in cm s^{-1} of Run 1a at 1200 LST, using a contour interval of 10 cm s^{-1}.

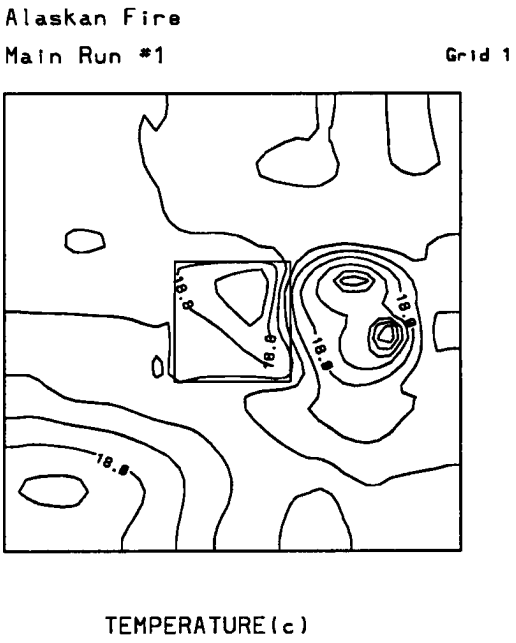

Figure 4.41: Temperature field (°C) of Run 1 at 1200 LST at 16.8 m AGL, using a contour interval of 0.2°C.

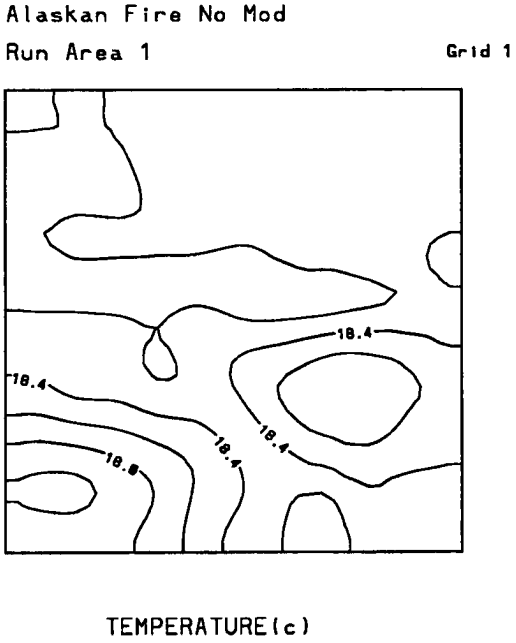

Figure 4.42: Temperature field (°C) of Run 1a at 1200 LST at 16.8 m AGL, using a contour interval of 0.2°C.

Both comparisons of upward vertical velocity and temperature fields show the effect of placing the burn area in the center of the model domain. By 1200 LST, the simulation containing the burn area has developed a strong circulation center just to the east of the burn area, while the unmodified simulation shows no sign of any circulation. This continues through 1600 LST. The temperature fields are similar, with no concentrated area of warming noticeable by 1200 LST in the unmodified simulation. No strong area of cooling is evident in the unmodified simulation, as the strong downward vertical motions do not develop as they do in the burn area simulation. Figures 4.43 and 4.44 show the sensible heat flux across the model domain for Run 1 and Run 1a at 1200 LST. The effects of placing the lower albedo burn area in the model run are very apparent. The concentration of contours near the borders of the burn area are very evident. The maximum value of sensible heat flux is located in the burn area. One can also see the effects of the clouds to the east of the burn area lowering the flux values. Values in the non-modified run are basically terrain and solar position dependent, giving fairly uniform numbers across the domain.

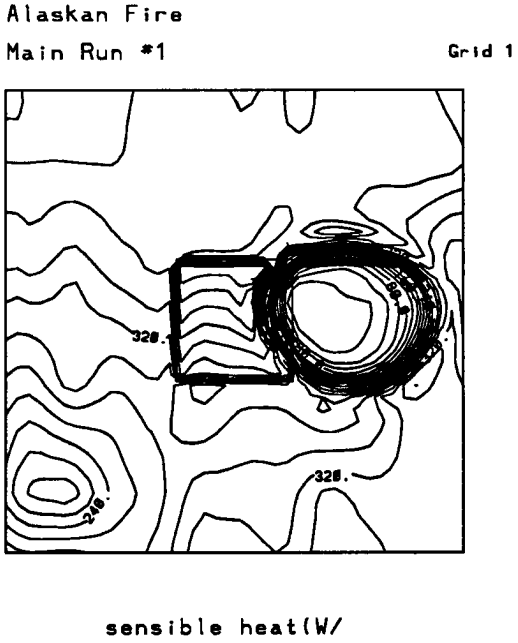

Figure 4.43: Sensible heat flux (W m^2) for Run 1 at 1200 LST, using a contour interval of 10 W m^2.

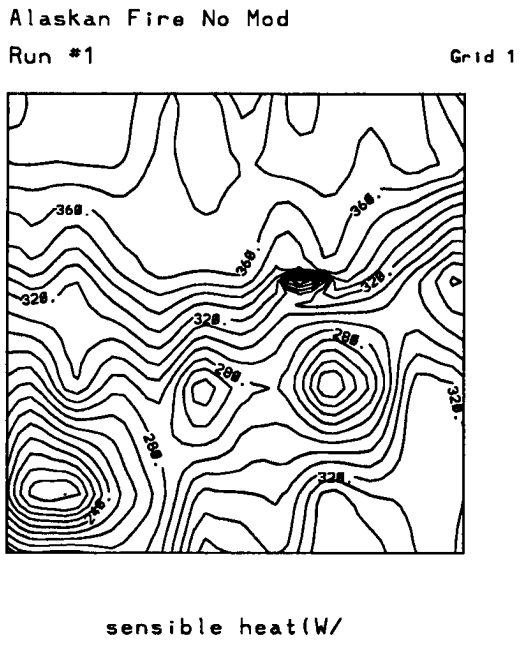

Figure 4.44: Sensible heat flux (W m^2) for Run 1a at 1200 LST, using a contour interval of 10 W m^2.

Figures 4.45 and 4.46 show the vertical velocity fields across the burn area for Run 2 (burn area) and Run 2a (non-burn area) at 1200 LST. Figures 4.47 and 4.48 show the near surface thermal structure of Runs 2 and 2a at 1200 LST. Figures 4.49 and 4.50 show the sensible heat fluxes of Runs 2 and 2a at 1200 LST.

The comparisons between the burn area and unmodified simulations in the case of Run 2 are very similar to those obtained in Run 1. No organized circulation center develops in the unmodified simulation while a strong circulation has developed by 1200 LST in the burn area simulation. Temperature fields continue the trend of no concentrated areas of warming or cooling noted in the unmodified simulation. Temperature rise throughout the simulation away from the burn area location is similar in both cases. The effects of the lower albedo yield similar results to those obtained with Run 1. A strong concentration of sensible heat flux contours can be seen around the burn area in the modified run, while the non-modified run shows fairly uniform values across the domain. Note also the higher sensible heat values on the higher terrain north of the burn area. Although not as high as the values obtained in the burn area, the higher terrain values are much greater than those at the lower elevations to the south.

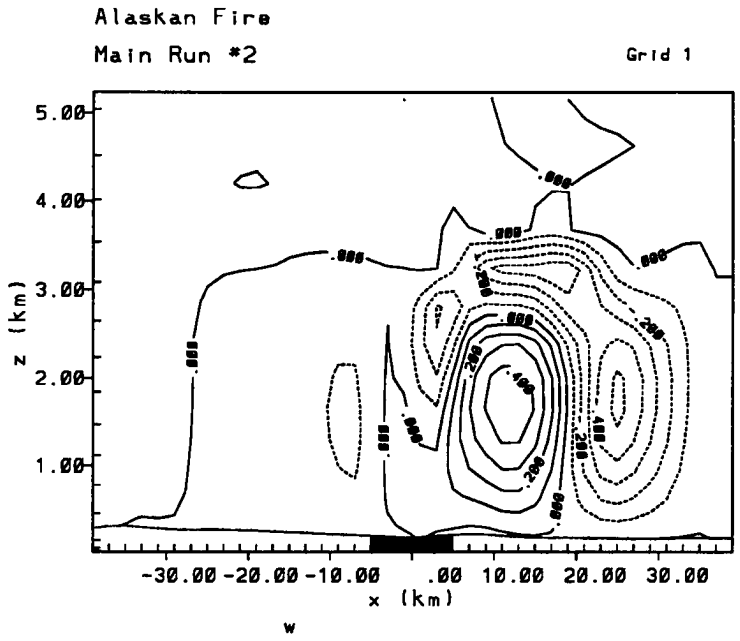

Figure 4.45: Vertical velocity field (w) in cm s^{-1} of Run 2 at 1200 LST, using a contour interval of 10 cm s^{-1}.

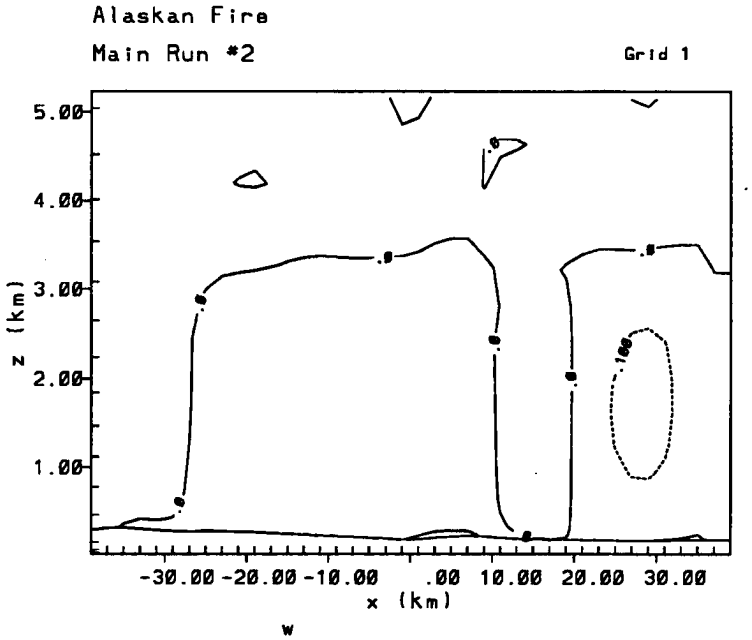

Figure 4.46: Vertical velocity field (w) in cm s^{-1} of Run 2a at 1200 LST, using a contour interval of 10 cm s^{-1}.

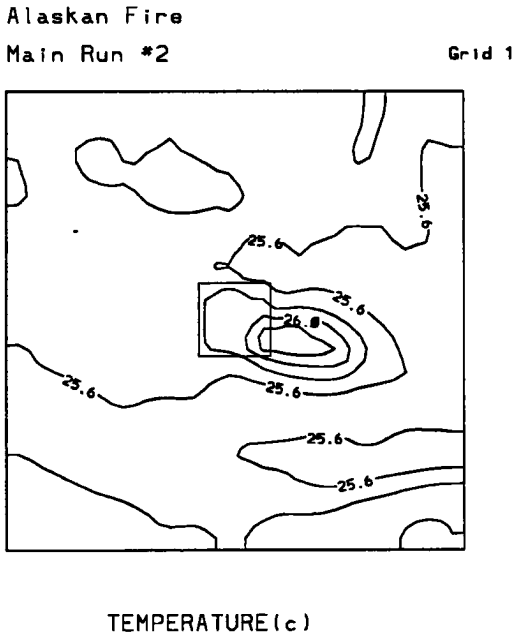

Figure 4.47: Temperature field (°C) of Run 2 at 1200 LST at 16.8 m AGL, using a contour interval of 0.2°C.

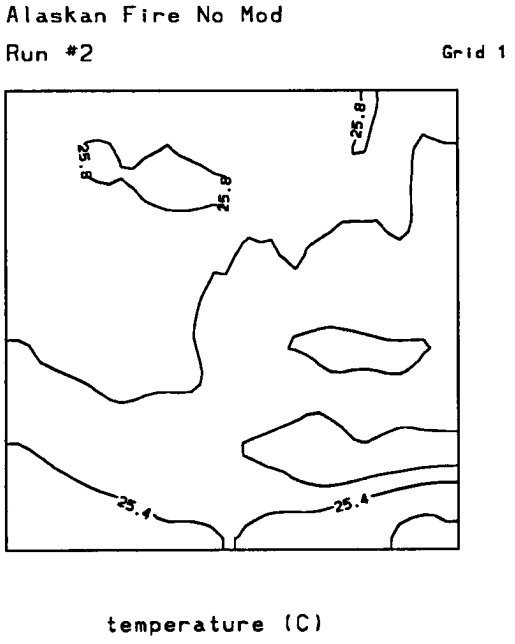

Figure 4.48: Temperature field (°C) of Run 2a at 1200 LST at 16.8 m AGL, using a contour interval of 0.2°C.

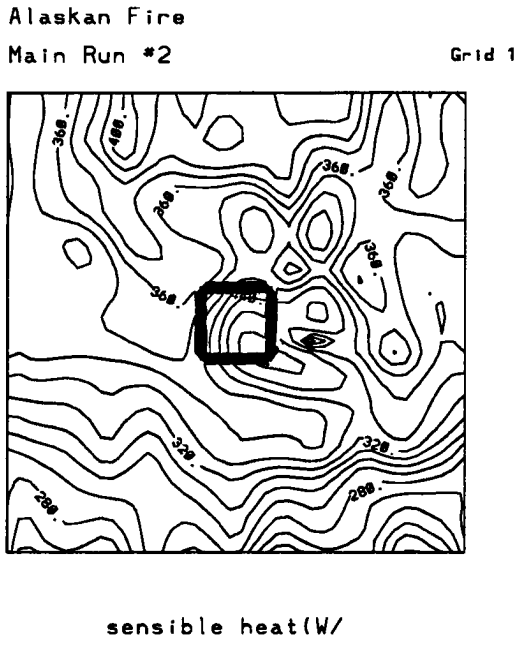

Figure 4.49: Sensible heat flux (W m^2) for Run 2 at 1200 LST, using a contour interval of 10 W m^2.

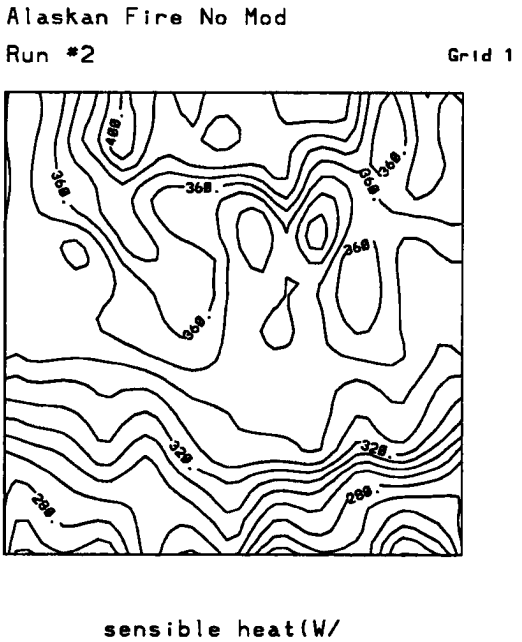

Figure 4.50: Sensible heat flux (W m^2) for Run 2a at 1200 LST, using a contour interval of 10 W m^2.

Chapter 5

SENSITIVITY EXPERIMENTS

The simulations are divided into four parts: 1) the effect of burn area size, 2) the effect of burn area albedo, 3) the effect of geostrophic wind, and 4) the effect of thermodynamic stability. A summary of the simulations is included as Table 5.1. The sensitivity runs use the 10-minute terrain data provided by USGS. The runs are centered at 65.0° N latitude and 147.8° W longitude. This is about 20 miles to the northwest of Fairbanks. Figure 5.1 shows an $x - y$ topographical plot of the simulation area. The model set-up for the sensitivity simulations are similar to the set-up used in the two main runs. There are 40 grid points in the x (east-west) direction, but only 1 grid point in the y (north-south) direction with a $\Delta x = 2$ km.

Table 5.1: Summary of Sensitivity Runs

Sensitivity Run	Burn Area (km^2)	Burn Area Albedo	U_g ($m\ s^{-1}$)	Vertical Stability
1a-b	100,400	0.05	0.0	Actual *
2a-b	400	0.05,0.10	0.0	Actual *
3a-c	100	0.05	-2.5,2.5,5.0	Actual *
4a-c	400	0.05	-2.5,2.5,5.0	Actual *
5a-c	100	0.10	-2.5,2.5,5.0	Actual *
6a-c	400	0.10	-2.5,2.5,5.0	Actual *
7a-b	100,400	0.05	0.0	2.5°C km^{-1}
8a-b	100,400	0.10	0.0	2.5°C km^{-1}
9a-b	100,400	0.05	0.0	9.0°C km^{-1}
10a-b	100,400	0.10	0.0	9.0°C km^{-1}

*RAOB sounding was from Fairbanks, Alaska, 21 June 1991 at 0Z

There are 15 vertical levels with a minimum stretched grid of 600 m ($\Delta z = 600$ m) near the ground and up to a maximum of grid increment of 800 m near the top of the

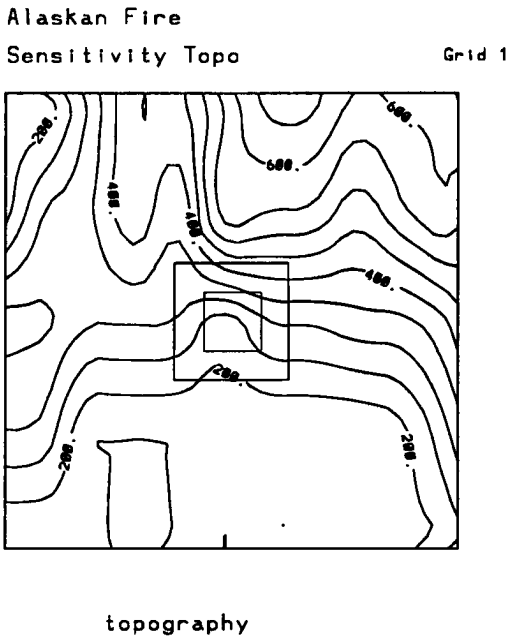

Figure 5.1: Topographical plot of the simulation area, using a contour interval of 50 m MSL.

model (11 km). The model time step is 3 seconds. All of the physical parameterizations are the same as used in the main run, with the exception of moisture. Vapor passive tracer is used instead of full microphysics that is utilized in the main runs. This will yield dry results. Only the generation and strength of the circulation center is being tested here, not the capability of the center to generate clouds.

5.1 The Effect of Burn Area Size

This initial set of simulations, Runs 1a-b, consider the relationship between the width of the burn area and the intensity of the mesoscale circulation. The circulation intensity can be measured by the magnitudes of velocity and the circulation height (Xian and Pielke, 1991). Each of the two simulations began to form weak circulation centers 1 hour after model start (0800 LST). The 100 sq km burn area had one circulation center, while the 400 sq km burn area had two circulation centers that formed along both sides of the burn area. These two circulation centers strengthen and expand until they merge over the center of the burn area at 1400 LST. Figures 5.2 and 5.3 illustrate the vertical velocities (w) at 1400 LST for the 100 and 400 sq km burn areas. In both cases, the peak vertical velocities

occur at 1400 LST, but the 400 sq km case has a larger maximum (3.5 m s^{-1}) than the 100 sq km case (2.75 m s^{-1}). This agrees with studies by Xian and Pielke (1991), and Yan and Anthes (1988). Both concluded that the strongest mesoscale generated vertical motions were produced by cases where two separate circulation centers merge near the time of maximum boundary layer heating at the center of the landmass (burn area). Figures 5.4 and 5.5 illustrate the horizontal flow pattern associated with the circulations, while Figures 5.6 and 5.7 illustrate the thermal structure of the circulations. Figure 5.8 depicts the diurnal variation of the peak values of vertical velocities among the two runs.

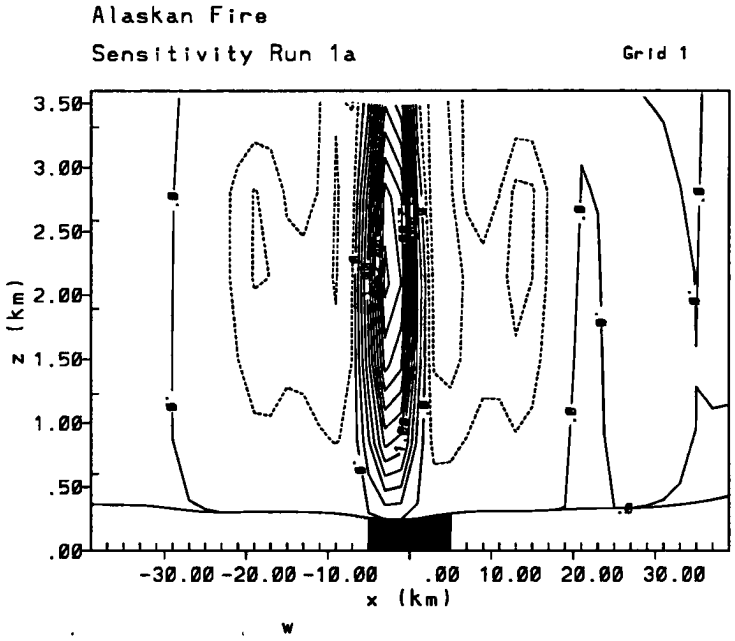

Figure 5.2: Vertical velocity field (w) in cm s^{-1} of Run 1a for a burn area of 100 sq km at 1400 LST, using a contour interval of 25 cm s^{-1}.

5.2 The Effect of Albedo

The previous experiments considered the influence of the burn area size on the development and intensity of the mesoscale circulation. Here, we will show the role that the albedo can play in strengthening/weakening the development of the circulation. The circulation intensity will again be measured by the magnitude of vertical motion and circulation height. This set of experiments, Runs 2a-b (see Table 5.1), used an albedo of 0.05 for the burn area, and an albedo of 0.15 for the surrounding area. If we increase the

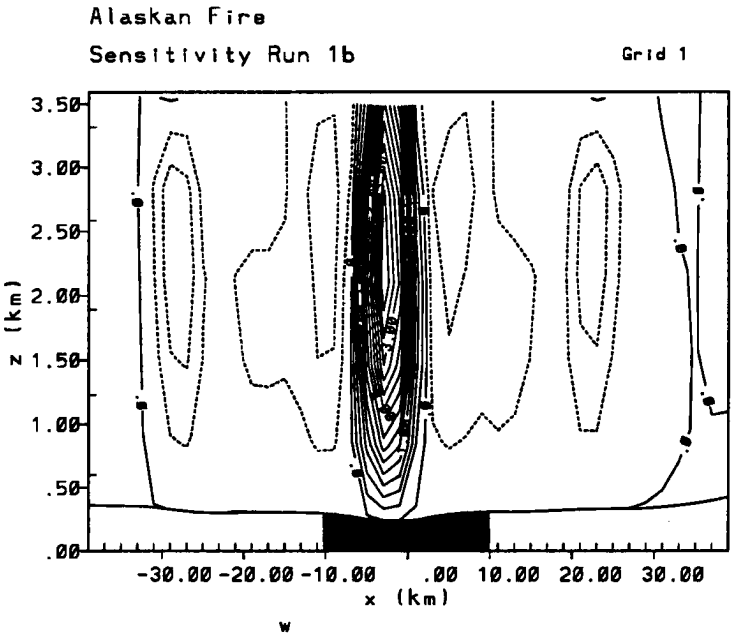

Figure 5.3: Vertical velocity field (w) in cm s^{-1} of Run 1b for a burn area of 400 sq km at 1400 LST, using a contour interval of 25 cm s^{-1}.

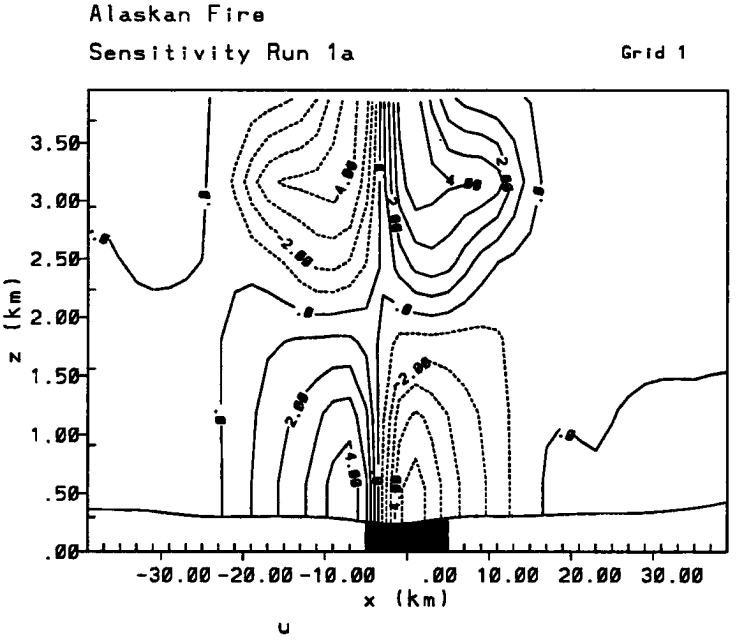

Figure 5.4: Horizontal velocity U component in m s^{-1} of Run 1a at 1400 LST, using a contour interval of 1 m s^{-1}.

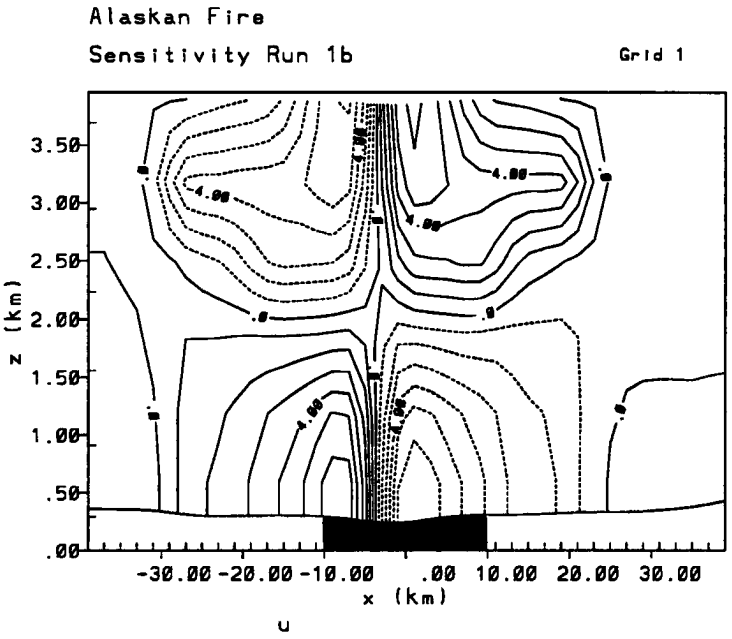

Figure 5.5: Horizontal velocity U component in m s^{-1} of Run 1b at 1400 LST, using a contour interval of 1 m s^{-1}.

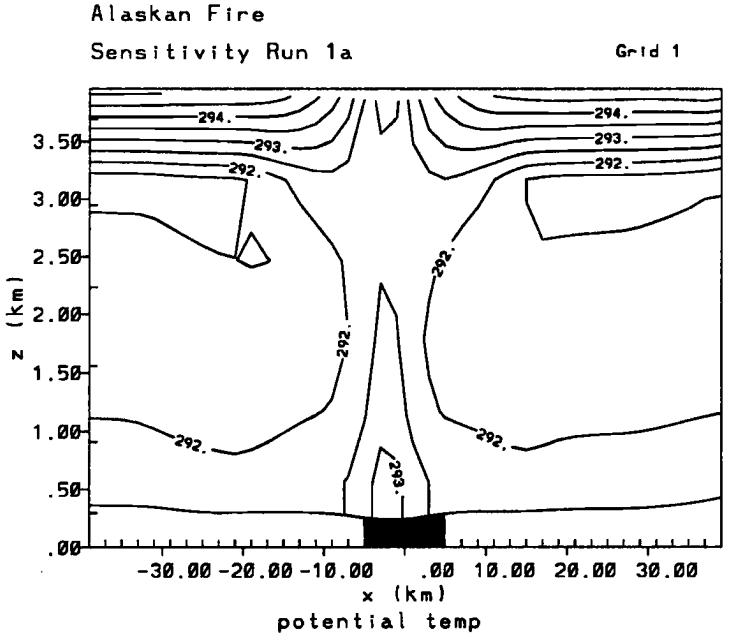

Figure 5.6: Potential temperature field (θ) for Run 1a at 1400 LST, using a contour interval of 0.25°C.

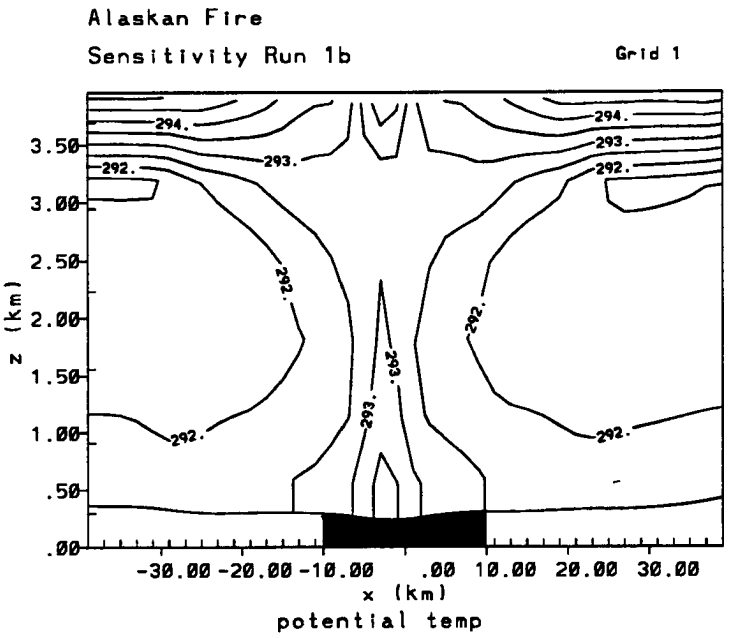

Figure 5.7: Potential temperature field (θ) for Run 1b at 1400 LST, using a contour interval of 0.25°C.

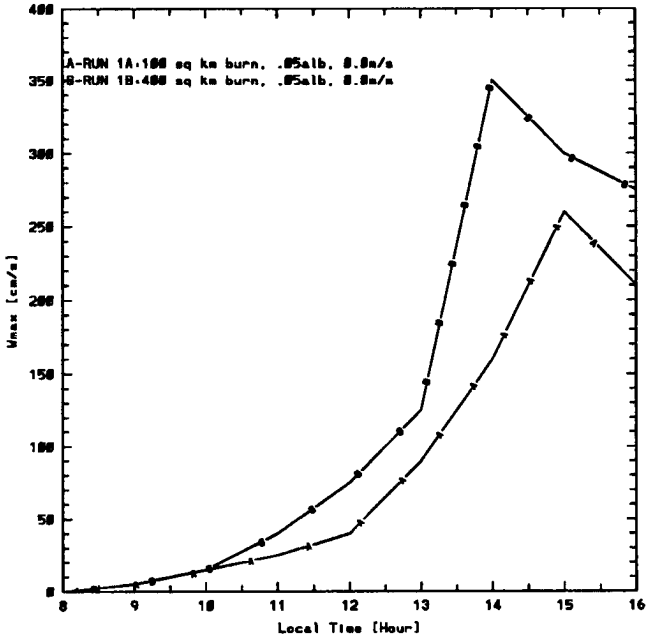

Figure 5.8: Diurnal variation of maximum vertical velocity for Runs 1a and b.

albedo of the burn area from 0.05 to 0.10, corresponding to a) the regrowth of vegetation in the burn area, or b) a lighter burn, some interesting results occur. In both cases, weak circulation centers generate along both sides of the 400 sq km burn area 1 hour after the start of the simulation (0800 LST). Both cases strengthen and expand until they merge over the center of the burn area. The 0.05 albedo case, however, merges 1 hour earlier (1400 LST) than the 0.10 case. The 0.05 albedo case's vertical velocity maximum is also stronger (3.50 m s^{-1}) than the 0.10 albedo case (2.75 m s^{-1}). Figures 5.9 and 5.10 present the vertical velocities (w) at 1400 LST for the 0.05 albedo case at 1600 LST for the 0.10 albedo case. This matches the results by Xian and Pielke (1991) that showed that late afternoon merging circulations have weaker intensities than circulations that merge during the mid afternoon. Figures 5.11 and 5.12 illustrate the horizontal flow associated with the circulations, while Figures 5.13 and 5.14 illustrate the thermal structure of the circulations. Figure 5.15 depicts the diurnal variation of the peak values of vertical velocities among the two runs.

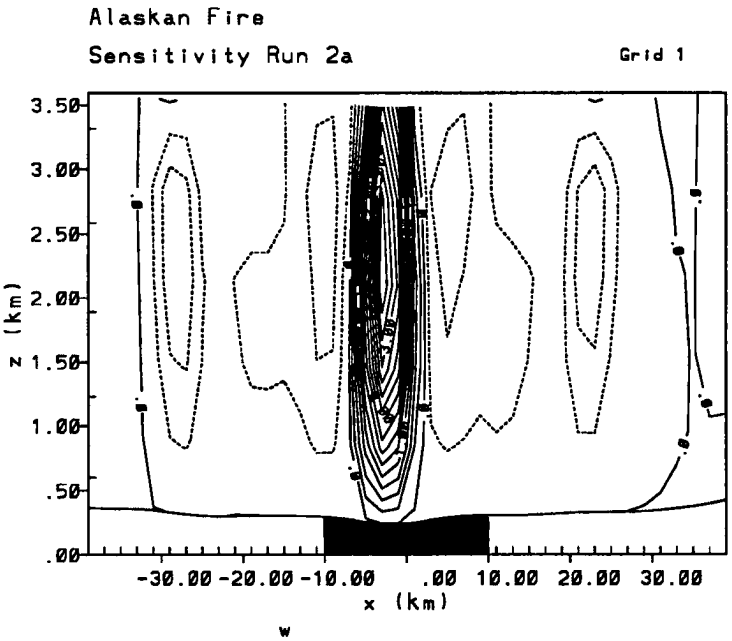

Figure 5.9: Vertical velocity field (w) in cm s^{-1} of Run 2a for a burn area albedo of 0.05 at 1400 LST, using a contour interval of 25 cm s^{-1}.

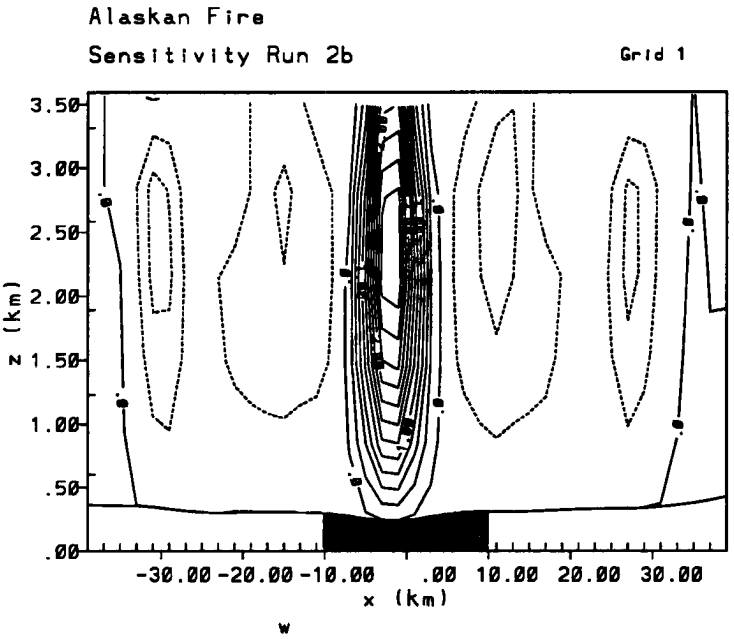

Figure 5.10: Vertical velocity field (w) in cm s^{-1} of Run 2b for a burn area albedo of 0.10 at 1600 LST, using a contour interval of 25 cm s^{-1}.

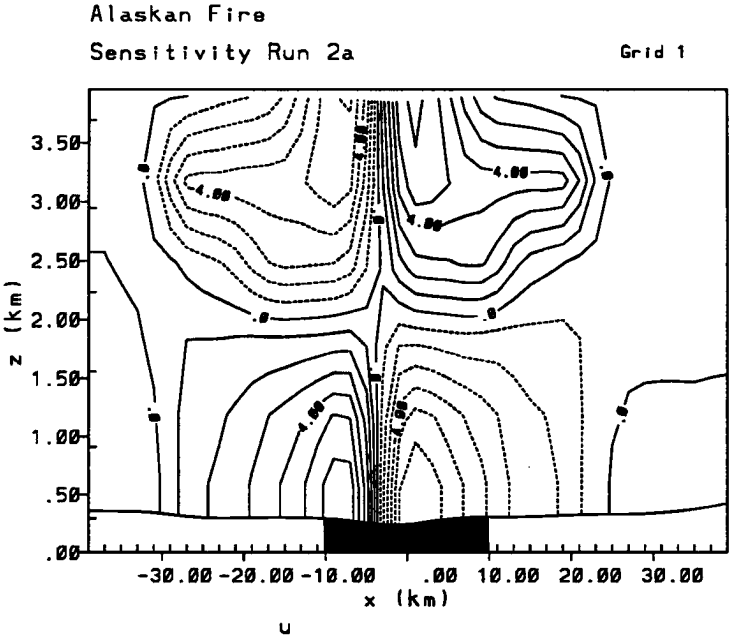

Figure 5.11: Horizontal velocity U component in m s^{-1} of Run 2a at 1400 LST, using a contour interval of 1 m s^{-1}.

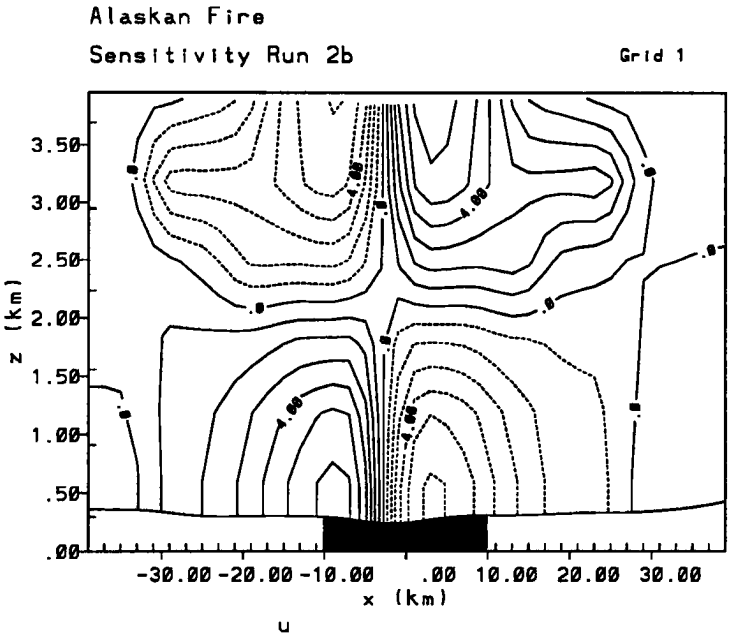

Figure 5.12: Horizontal velocity U component in m s^{-1} of Run 2b at 1600 LST, using a contour interval of 1 m s^{-1}.

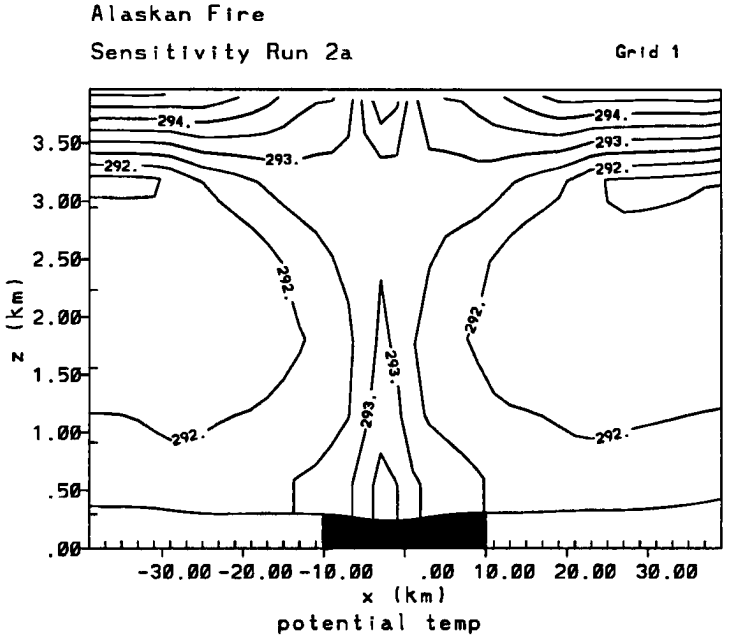

Figure 5.13: Potential temperature field (θ) for Run 2a at 1400 LST, using a contour interval of 0.25°C.

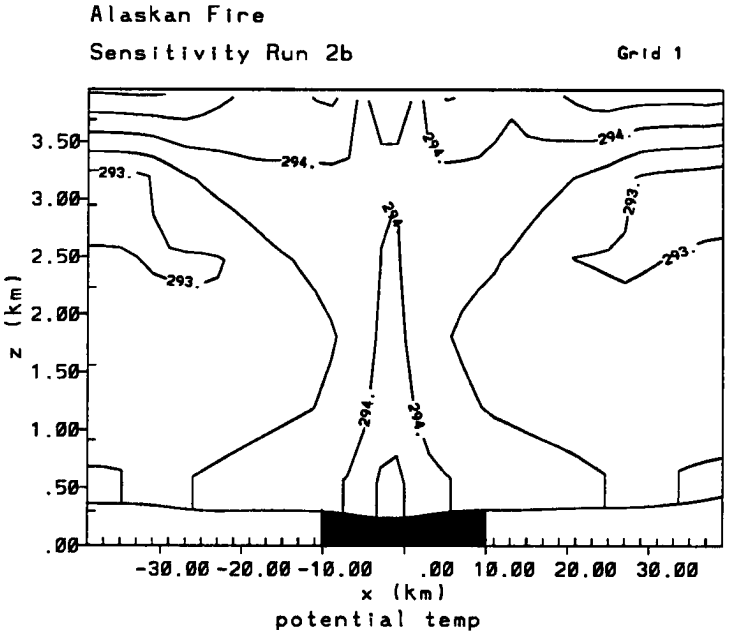

Figure 5.14: Potential temperature field (θ) for Run 2b at 1600 LST, using a contour interval of 0.25°C.

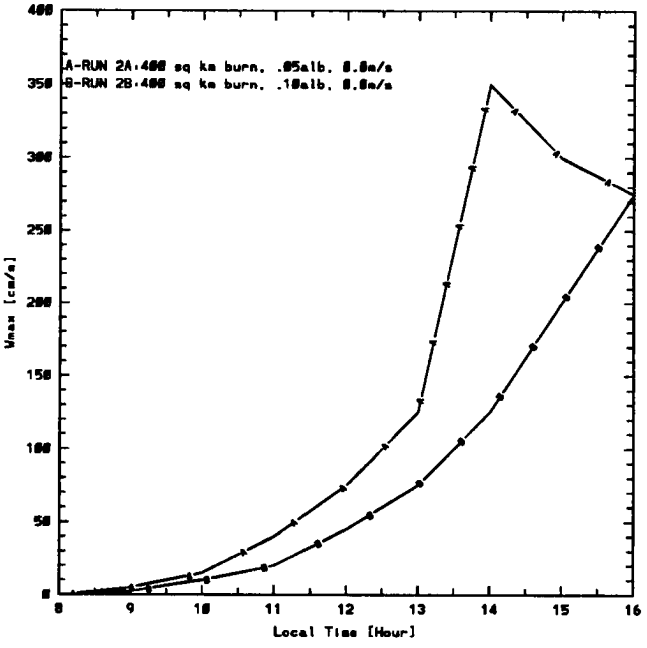

Figure 5.15: Diurnal variation of maximum vertical velocity for Runs 2a and b.

5.3 The Effect of Geostrophic Wind

From the previous experiments we know that the maximum vertical velocities are related to the width of the burn area along with the burn area albedo. This set of experiments, Runs 3a-6c (see Table 5.1), explore the influence of the geostrophic wind on the development and intensity of the mesoscale circulation. The model was initialized with geostrophic westerly winds of $U_g = -2.5$ (an easterly wind), 2.5, and 5.0 m s^{-1}. Burn area widths of 100 and 400 sq km along with burn area albedos of 0.05 and 0.10 were used for these sets of experiments. Xian and Pielke (1991), along with Arritt (1993) showed how the maximum intensity and structure of vertical motion associated with sea breezes will change with differing values of large-scale flow. Both studies showed that sea breeze circulations were weakened considerably when the large-scale flow exceeded a few meters per second, especially in the cases where the landmass size was $\leq$50 km. The first set of geostrophic flow sensitivity experiments had geostrophic flow of $U_g = -2.5$ m s^{-1}. This shows the effects of light easterly flow on the development of the mesoscale circulation. The maximum vertical velocities range from 0.075 to 0.375 m s^{-1}. Figure 5.16 shows the strongest vertical velocities (w) in Run 4a. Some very interesting features are apparent. The main circulation center develops on the west side of the burn area and slowly drifts to the west until by 1400 LST it is 20 km west of the burn area center. This is similar to the results of Runs 3b, 4b, 5b, and 6b, although the maximum vertical velocities are much less in the easterly runs. The reason that the velocities are much less in the easterly runs is that the terrain used in the simulations is conducive to westerly flow. The orientation of the terrain causes a reduction in the vertical development during the easterly cases. Figure 5.17 represents the w component for $U_g = 2.5$ m s^{-1} and a burn area width of 400 sq km along with a burn area albedo of 0.05 at 1400 LST (Run 4b). The mesoscale circulation has propagated approximately 25 km to the east of the central burn area. The maximum vertical velocity, w_{max}, in this case is 2.6 m s^{-1}. As was the case with Run 1a, the circulation center forms over the center of the burn area within 1 hour of simulation start (0800 LST). In the cases where U_g was chosen as 5.0 m s^{-1}, vertical velocities range from 0.05 to 0.10 m s^{-1}. Figure 5.18 shows the strongest vertical velocities (w) in Run 4c.

This low intensity of the circulation center indicates that the large-scale flow has almost eliminated the boundary layer thermal differences between the burned and unburned land areas. This is especially evident on the west side of the burn area. The only area that develops even a weak mesoscale circulation is to the east of the burn area. This correlates well with the results from Lyons and Cole (1976), Xian and Pielke (1991), and Arritt (1993). When the large-scale flow is $\geq$5 m s^{-1}, the mesoscale circulation is very shallow and on only one side of the burn area. This is due to the horizontal pressure gradient generated by the differential heating being insufficient to overcome the kinetic energy of the large-scale flow. Figures 5.19–5.21 illustrates the thermal structure of runs 4a-c. A summary of the diurnal variation of w for the each specific geostrophic wind case is given in Figures 5.22–5.24. Figure 5.25 contains a plot of the diurnal variation of w for $U_g = -2.5$, 0.0, 2.5, and 5.0 m s^{-1} along with a burn area width of 400 sq km and a burn area albedo of 0.05.

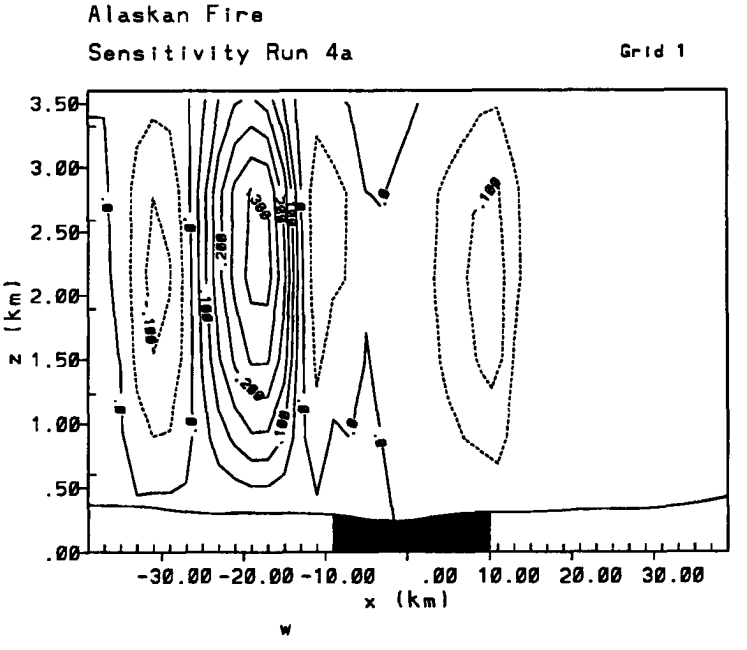

Figure 5.16: Vertical velocity field (w) in cm s^{-1} of Run 4a using $U_g = -2.5$ m s^{-1} at 1400 LST, using a contour interval of 10 cm s^{-1}.

5.4 The Effect of Thermodynamic Stability

In the previous experiments, we considered the role of wind speed/direction, along with albedo effects and burn area size. Here, we will concentrate on atmospheric forcing.

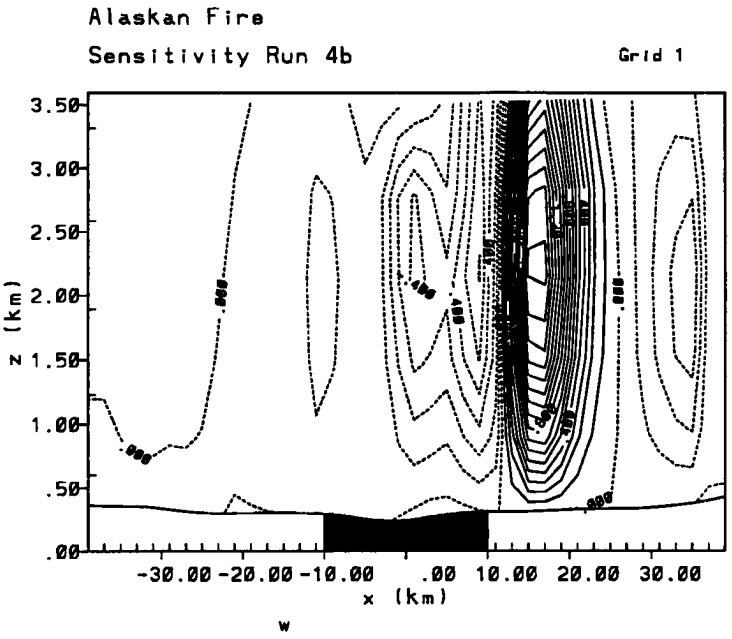

Figure 5.17: Vertical velocity field (w) in cm s^{-1} of Run 4b using $U_g = 2.5$ m s^{-1} at 1400 LST, using a contour interval of 10 cm s^{-1}.

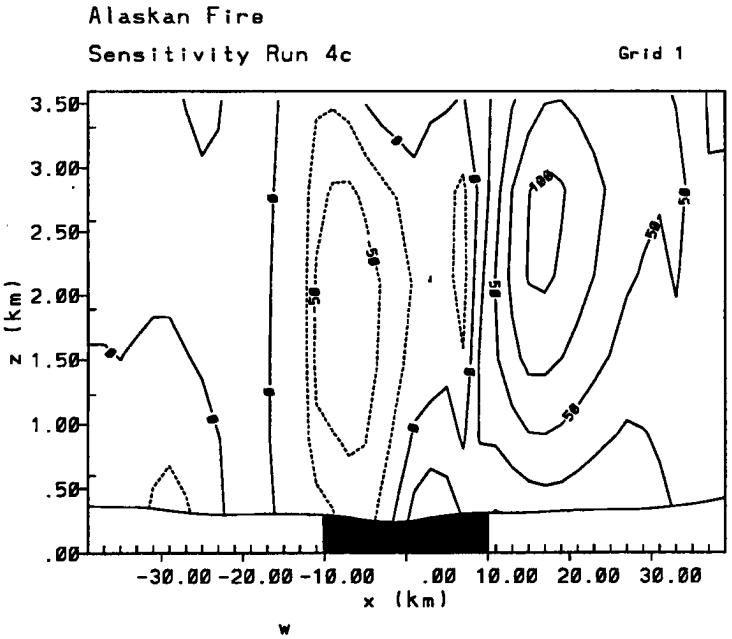

Figure 5.18: Vertical velocity field (w) in cm s^{-1} of Run 4c using $U_g = 5.0$ m s^{-1} at 1400 LST, using a contour interval of 5 cm s^{-1}.

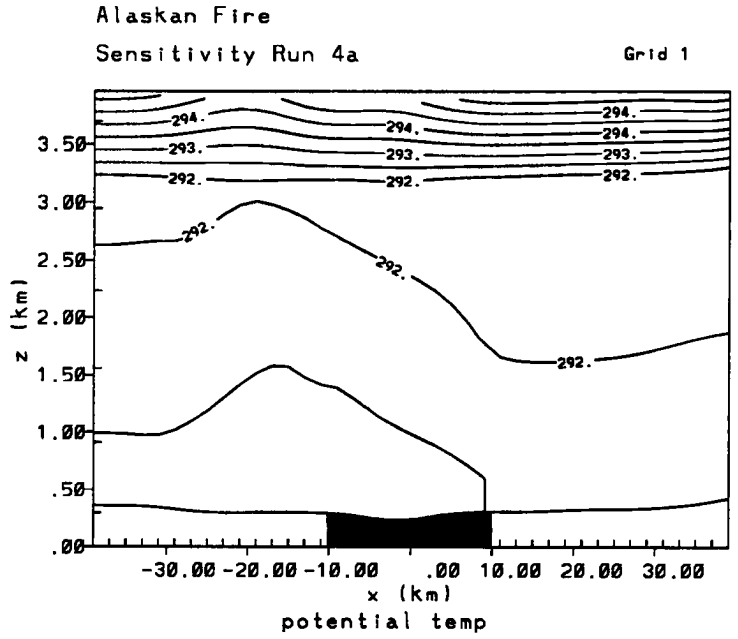

Figure 5.19: Potential temperature field (θ) of Run 4a using $U_g = -2.5$ m s^{-1} at 1400 LST, using a contour interval of 0.25°C.

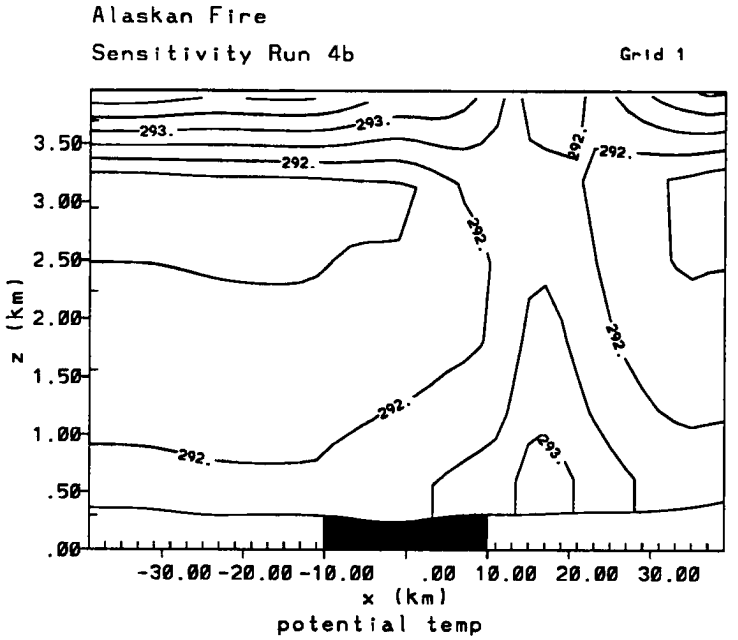

Figure 5.20: Potential temperature field (θ) of Run 4b using $U_g = 2.5$ m s^{-1} at 1400 LST, using a contour interval of 0.25°C.

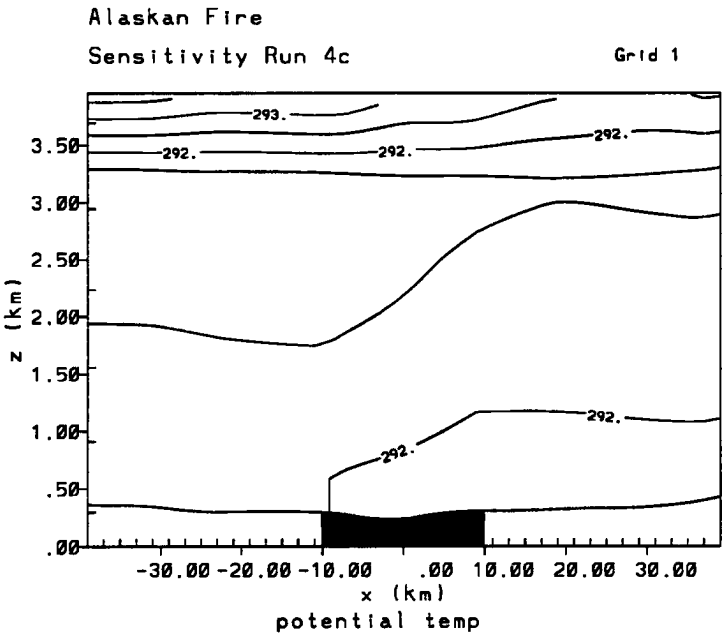

Figure 5.21: Potential temperature field (θ) of Run 4c using $U_g = 5.0$ m s^{-1} at 1400 LST, using a contour interval of 0.25°C.

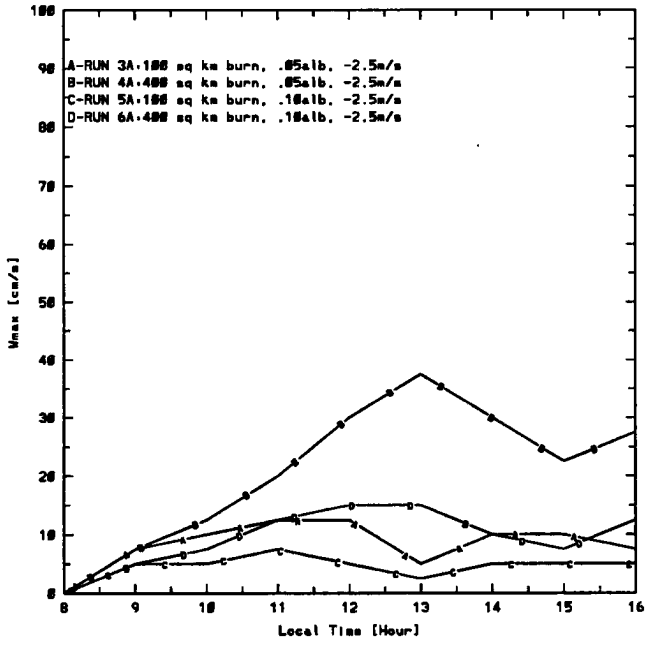

Figure 5.22: Diurnal variation of the vertical velocity field (w) for $U_g = -2.5$ m s^{-1} geostrophic wind runs.

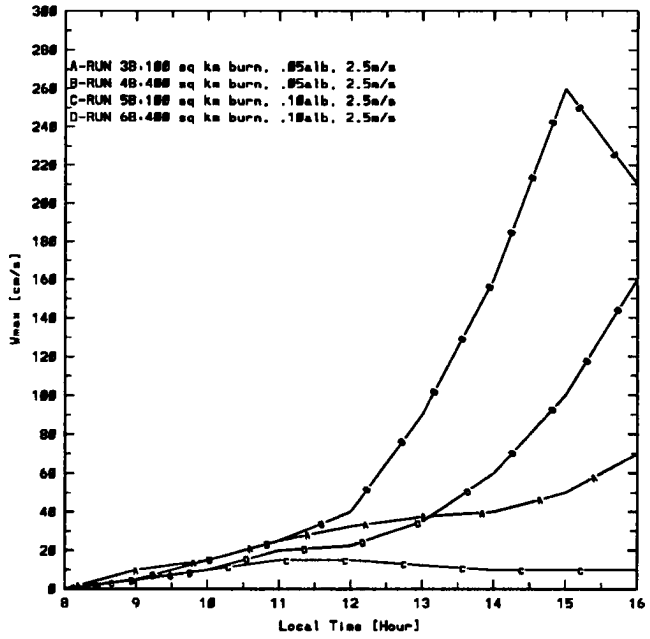

Figure 5.23: Diurnal variation of the vertical velocity field (w) for U_g = 2.5 m s^{-1} geostrophic wind runs.

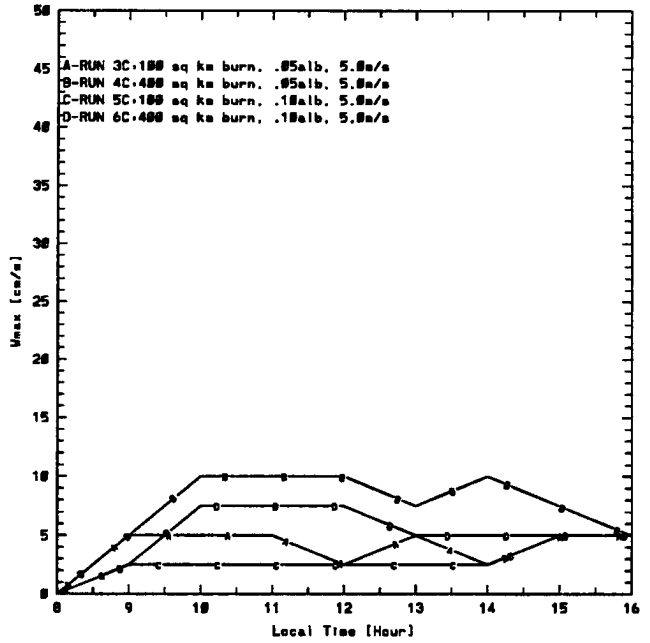

Figure 5.24: Diurnal variation of the vertical velocity field (w) for U_g=5.0 m s^{-1} geostrophic wind runs.

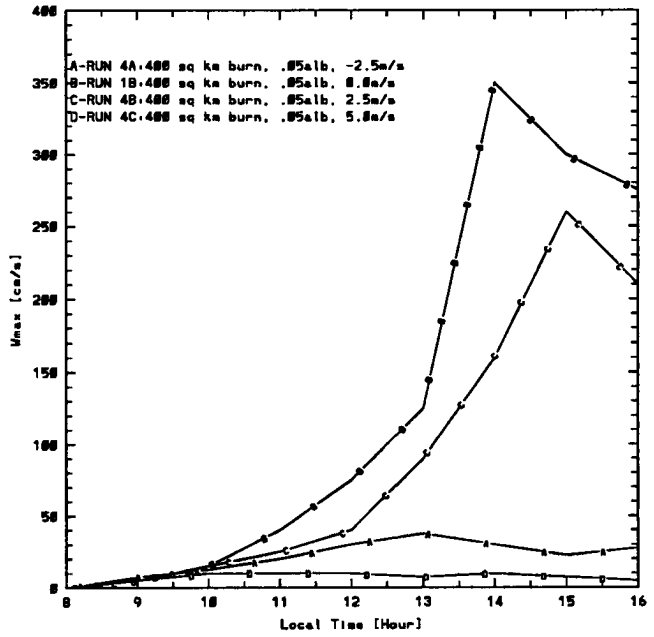

Figure 5.25: Diurnal variation of the vertical velocity field (w) for U_g = −2.5, 0.0, 2.5, and 5.0 m s^{-1} with burn area width/albedo = 400 sq km/0.05.

Atmospheric stability is an important factor for the development of the mesoscale circulation (Atkinson, 1981; Rotunno, 1983). This set of experiments, Runs 7a-10b (see Table 5.1), uses two separate initial thermal structures, $\frac{\partial \theta}{\partial z}$ = 2.5°C km^{-1} and = 9.0°C km^{-1}, respectively. We will let these values represent a stable and near-neutral static stability condition (Xian and Pielke, 1991). The influence of these conditions on the atmosphere and the development of the mesoscale circulation is evaluated. We will use an initial wind speed of 0.0 m s^{-1} and burn area widths of 100 and 400 sq km. Burn area albedos of 0.05 and 0.10 are also used. Figure 5.26 shows the strongest vertical velocities in Run 7b at 1600 LST. A maximum vertical velocity of 2.9 m s^{-1} has developed over the center of the burn area. The resulting U component along with the thermal structure are illustrated in Figures 5.27 and 5.28. When the thermal gradient is increased to 9.0°C km^{-1}, the resulting mesoscale circulation is much weaker. Figure 5.29 shows the maximum vertical velocity in Run 9b to be 0.175 m s^{-1} at 1600 LST. Two separate internal maxima develop on both the east and west sides of the mesoscale circulation, but they are much weaker than the two that develop in Run 7b and they also develop much later in the day. Again, the U component along with the thermal structure are plotted in Figures 5.30 and 5.31.

Figure 5.32 shows the peak values of vertical velocity for all of the thermodynamic stability runs. The values for w are all larger for the runs where $\frac{\partial \theta}{\partial z} = 2.5°C\ k^{-1}$ then when the gradient is $9.0°C\ km^{-1}$. These results are very similar to those obtained by Xian and Pielke (1991), and shows the effect that a stable atmosphere can have on the vertical and horizontal development of a mesoscale circulation. Also of note is that the strength of the circulation, in the cases where $\frac{\partial \theta}{\partial z} = 9.0°C\ k^{-1}$, does not depend on the size or albedo of the burn area. Figure 5.33 shows the peak values of vertical velocity for differing stabilities, but the same burn area and albedo. The strongest circulation develops in the weaker stratified atmosphere, in this case, the actual Fairbanks sounding, followed by the 2.5°C and the 9.0°C stability runs. These results are again similar to those found by Xian and Pielke (1991), Anthes (1978), Song et al. (1985), and Martin and Pielke (1983).

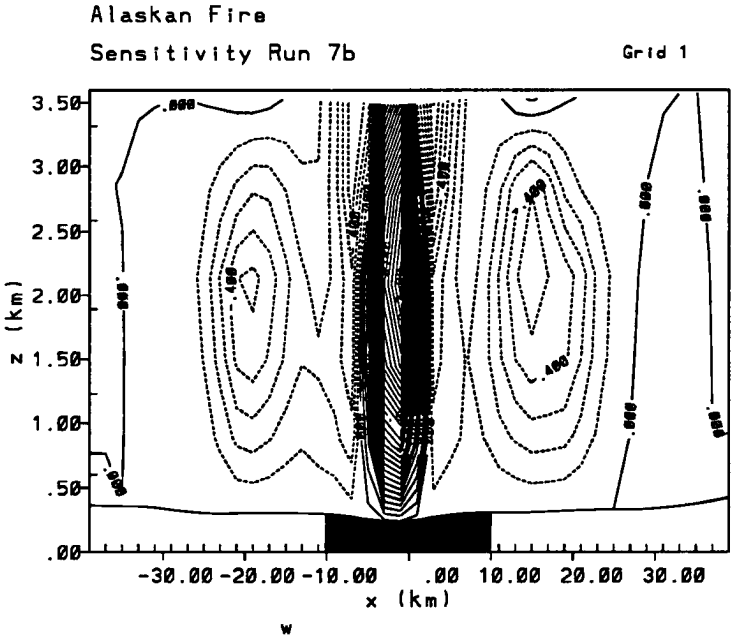

Figure 5.26: Vertical velocity field (w) in cm s^{-1} of Run 7b for a $\frac{\partial \theta}{\partial z}$=2.5°C k^{-1} at 1600 LST, using a contour interval of 10 cm s^{-1}.

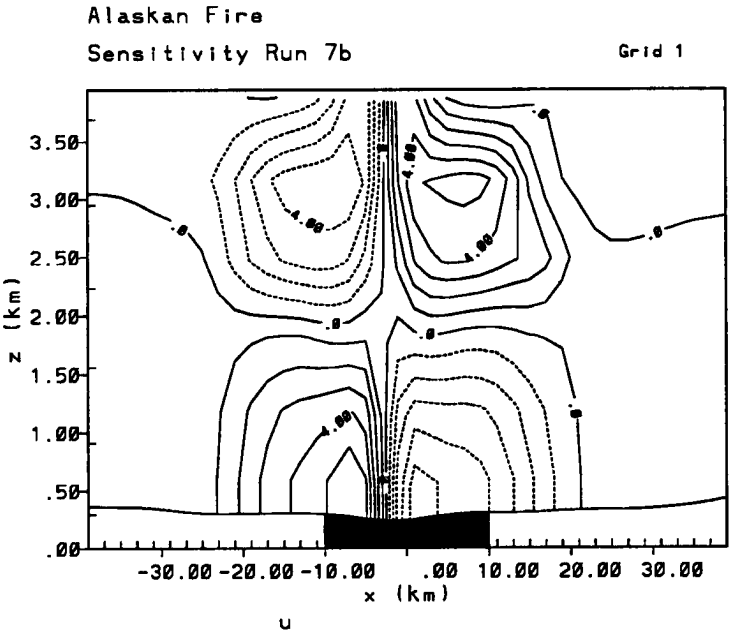

Figure 5.27: Horizontal velocity U component in m s^{-1} of Run 7b at 1600 LST, using a contour interval of 1 m s^{-1}.

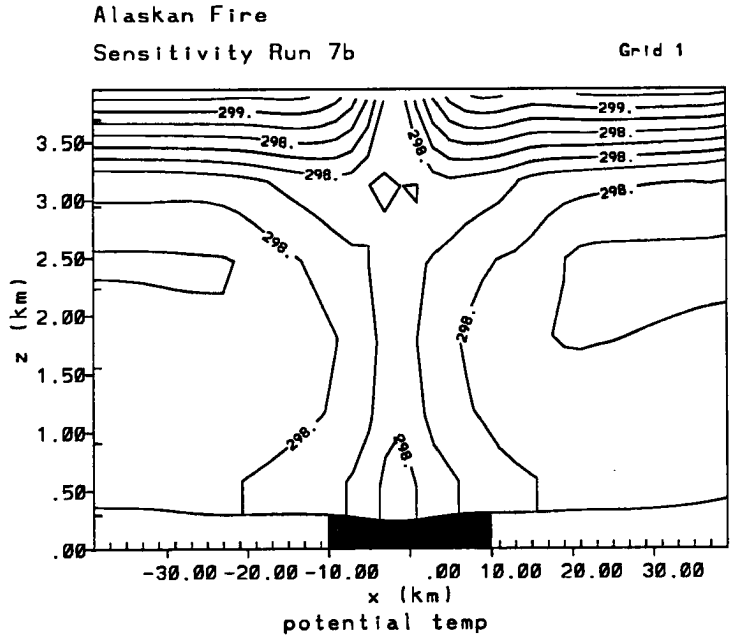

Figure 5.28: Potential temperature field (θ) of Run 7b at 1600 LST, using a contour interval of 0.25°C.

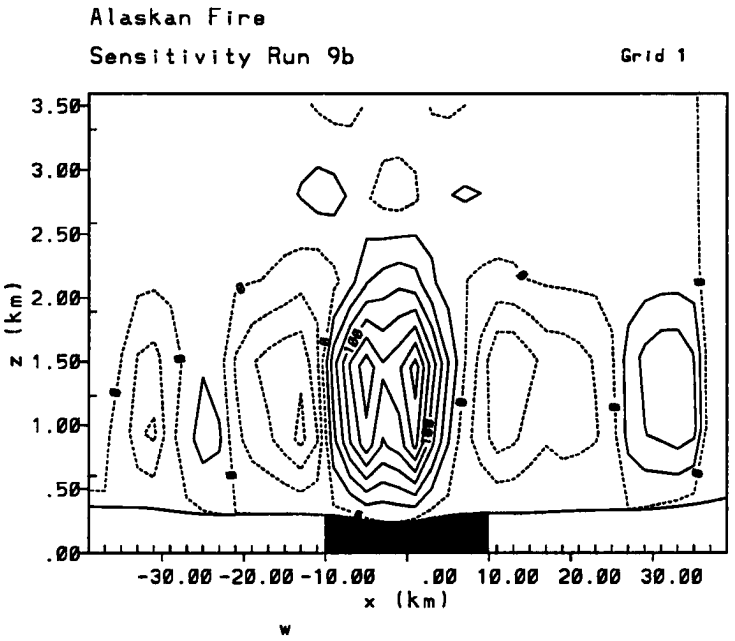

Figure 5.29: Vertical velocity field (w) in cm s^{-1} of Run 9b for a $\frac{\partial \theta}{\partial z}$=9.0°C k^{-1} at 1500 LST, using a contour interval of 2.5 cm s^{-1}.

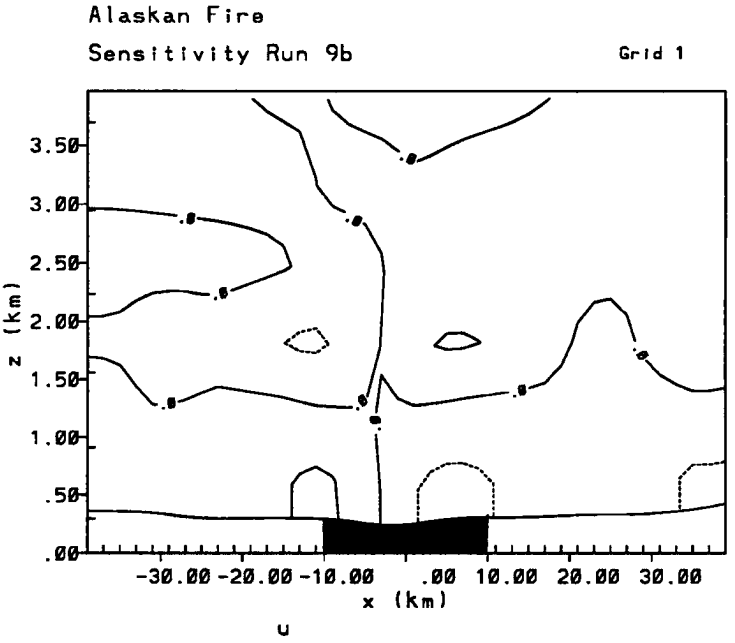

Figure 5.30: Horizontal velocity U component in m s^{-1} of Run 9b at 1500 LST, using a contour interval of 1 m s^{-1}.

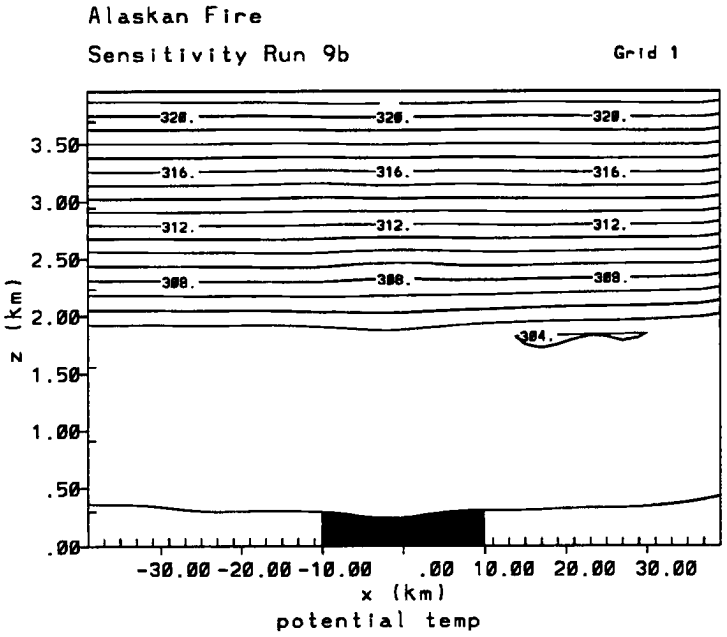

Figure 5.31: Potential temperature field (θ) of Run 9b at 1500 LST, using a contour interval of 0.25°C.

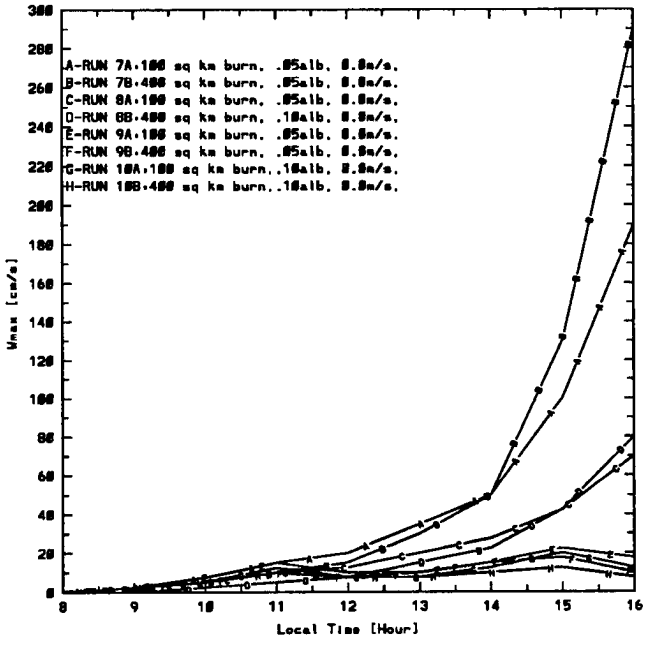

Figure 5.32: Diurnal variation of maximum vertical velocity for Runs 7a through 10b.

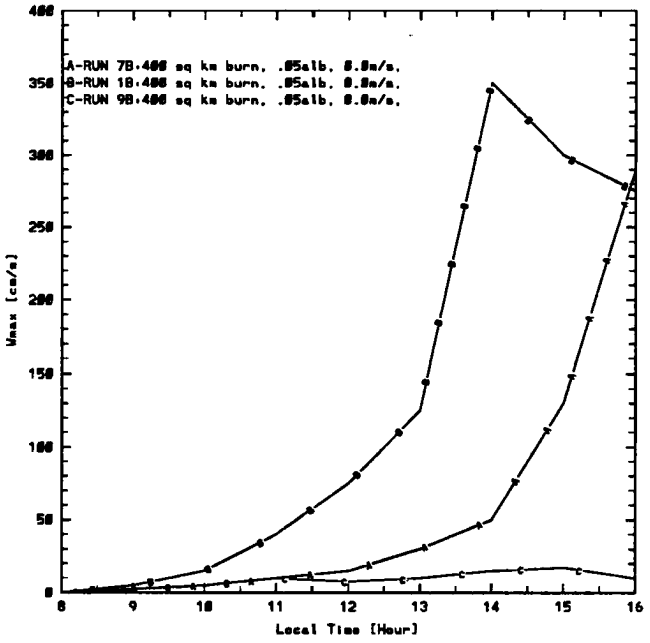

Figure 5.33: Diurnal variation of maximum vertical velocity for $\frac{\partial \theta}{\partial z} = 2.5°$, actual°C k^{-1}, and 9.0°C k^{-1}.

Chapter 6

LIGHTNING DATA

Data on lightning was provided courtesy of John Yarie (personal communication, 1993). There were over 2389 lightning strikes in the study area during the months of May through September 1988. The study area is centered at 66.83 N latitude and 144.82 W longitude, and is 304 km in the east-west direction and 228 km in the north-south direction. Figure 6.1 contains a topographical plot of the study area. Heights range from 100 m near the river basin to 1100 m in the northwest corner. The large box near the center is fire 1, and the smaller box to the north is fire 2. See Chapter 4 for fire specifics.

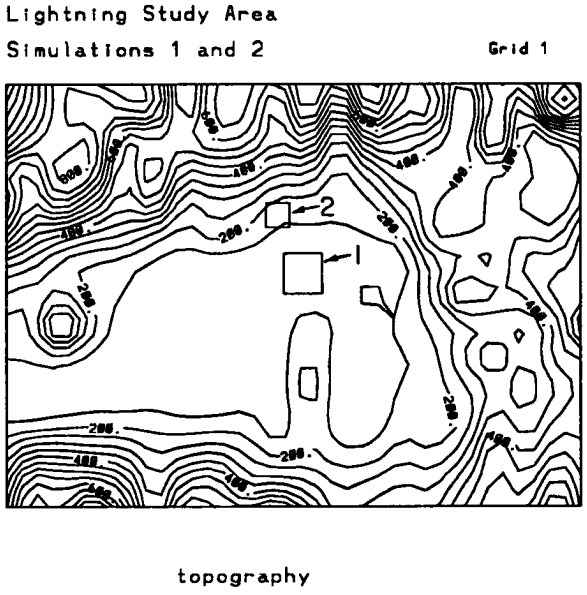

Figure 6.1: Topographical plot of the study area, using a contour interval of 50 m MSL.

Plots of lightning strikes during 1988 are illustrated in Figures 6.2 – 6.7. Figure 6.2 gives the locations of all 2389 lightning strikes along with the locations of all fires in the study area. Note that fires 433 and 577 were the fires used in the case study. These

fires are circled for convenience. Figure 6.3 gives the locations of all lightning strikes that occurred before Julian day 166, the start of fire 433. Figure 6.4 gives the locations of all lightning strikes that occurred after Julian day 166. Figure 6.5 gives the locations of all lightning strikes that occurred within 30 days of the start of fire 433. Figure 6.6 gives the locations of all lightning strikes that occurred after Julian day 197, the start of fire 577. Finally, Figure 6.7 gives the location of all lightning strikes that occurred within 30 days of the start of fire 577.

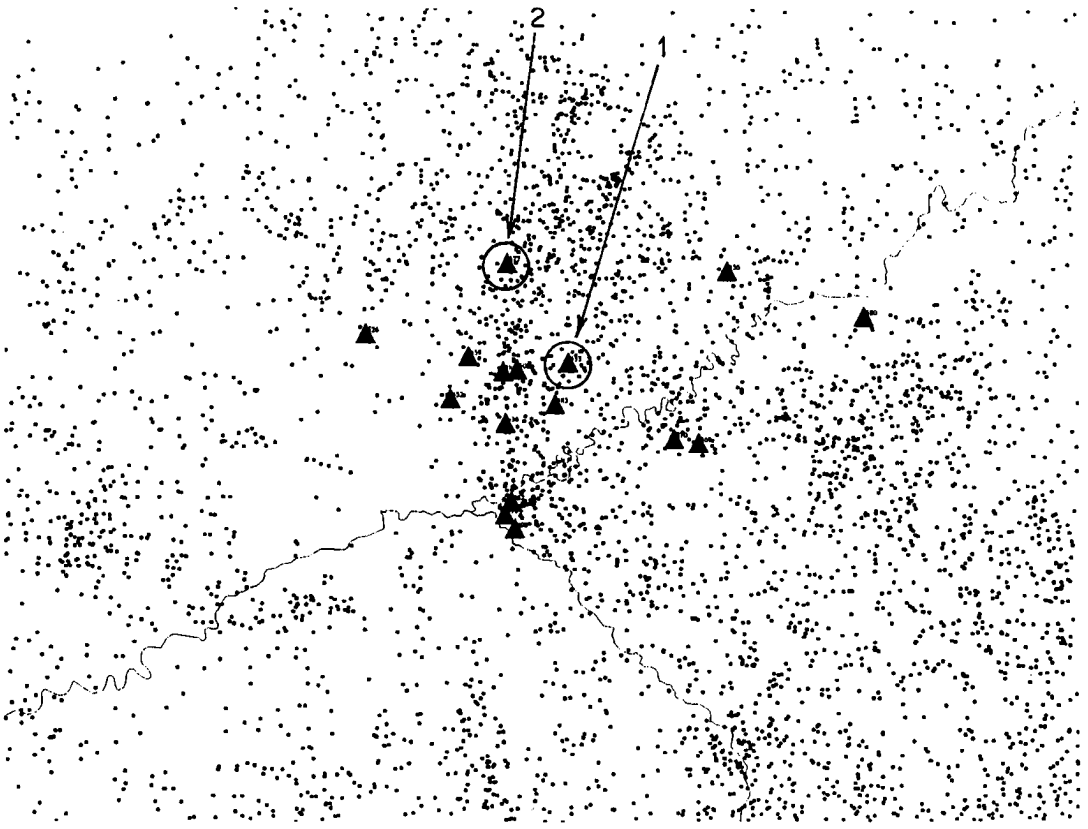

Figure 6.2: Lightning strike map of study area for 1988.

One can plainly see that the majority of the strikes occurred in the higher terrain surrounding the river valley. This makes sense given that the prevailing winds during the summer are from the southwest (early summer) to northwest (late summer), (Watson, 1974). The resultant upslope flow would help to orographically lift the available moisture to condensation. Thunderstorms would be the result of the lifted moisture. However, a large cluster of lightning strikes is visible in the area of the fires. This is interesting, as the terrain around the fires is basically flat. One possible explanation for this is the

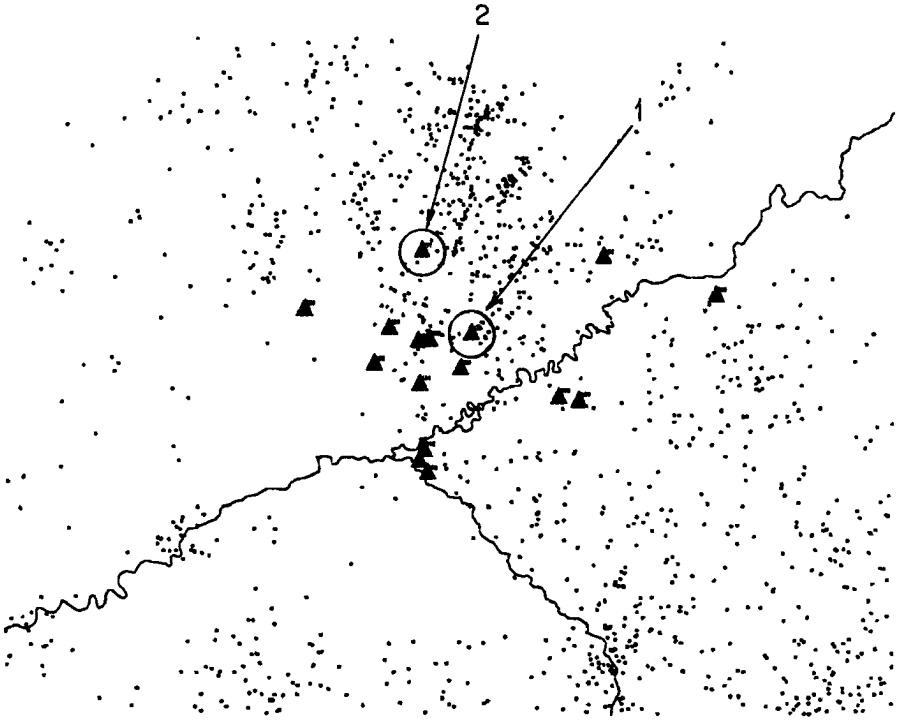

Figure 6.3: Lightning strike map of study area before Julian day 166.

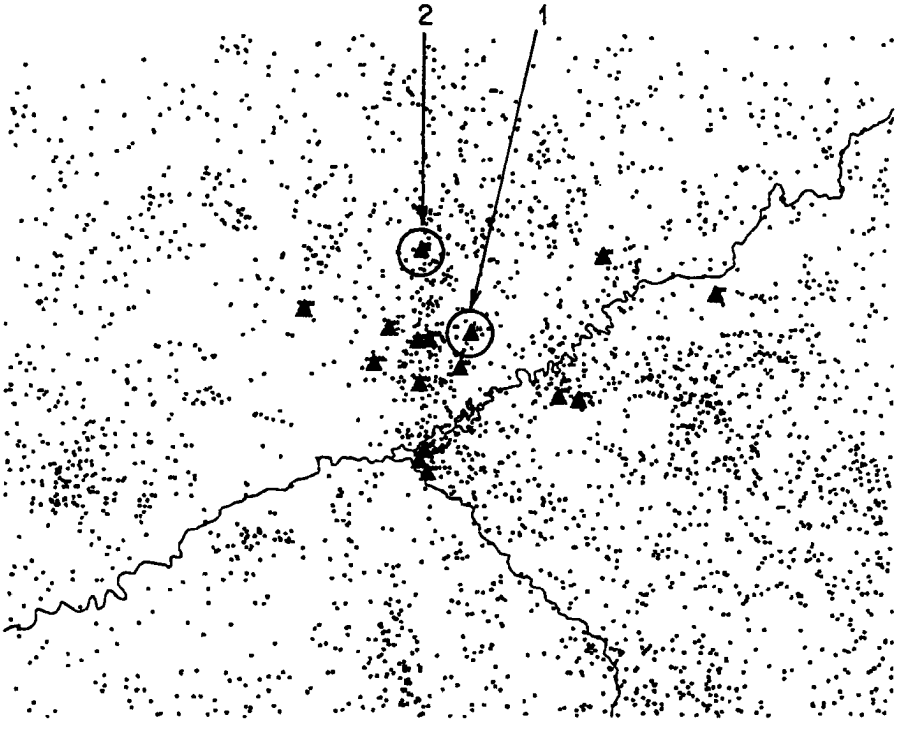

Figure 6.4: Lightning strike map of study area after Julian day 166.

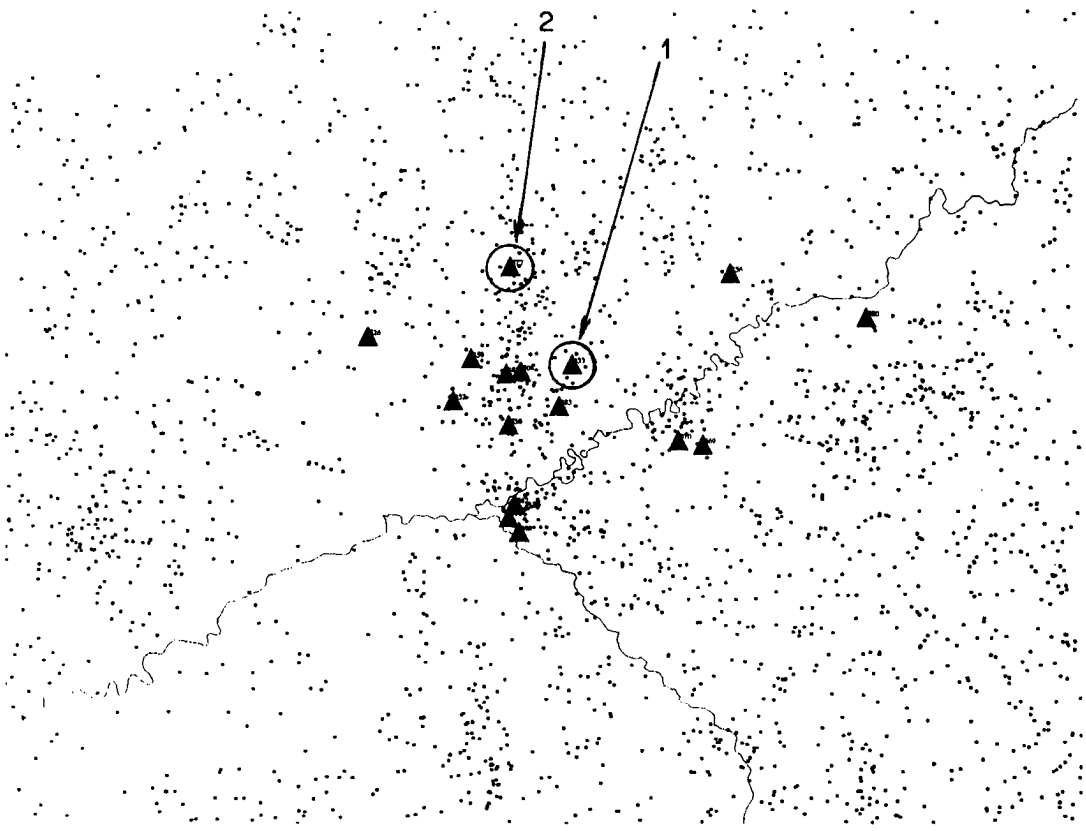

Figure 6.5: Lightning strike map of study area up to 30 days after Julian day 166.

development of mesoscale circulations from the albedo difference between the burned and unburned areas. The prevailing southwest to northwest winds would encounter the circulation center and clouds would develop from the vertical motions downwind of the burn areas. The ability of the certain sized circulation centers to produce clouds was shown in case studies 1 and 2.

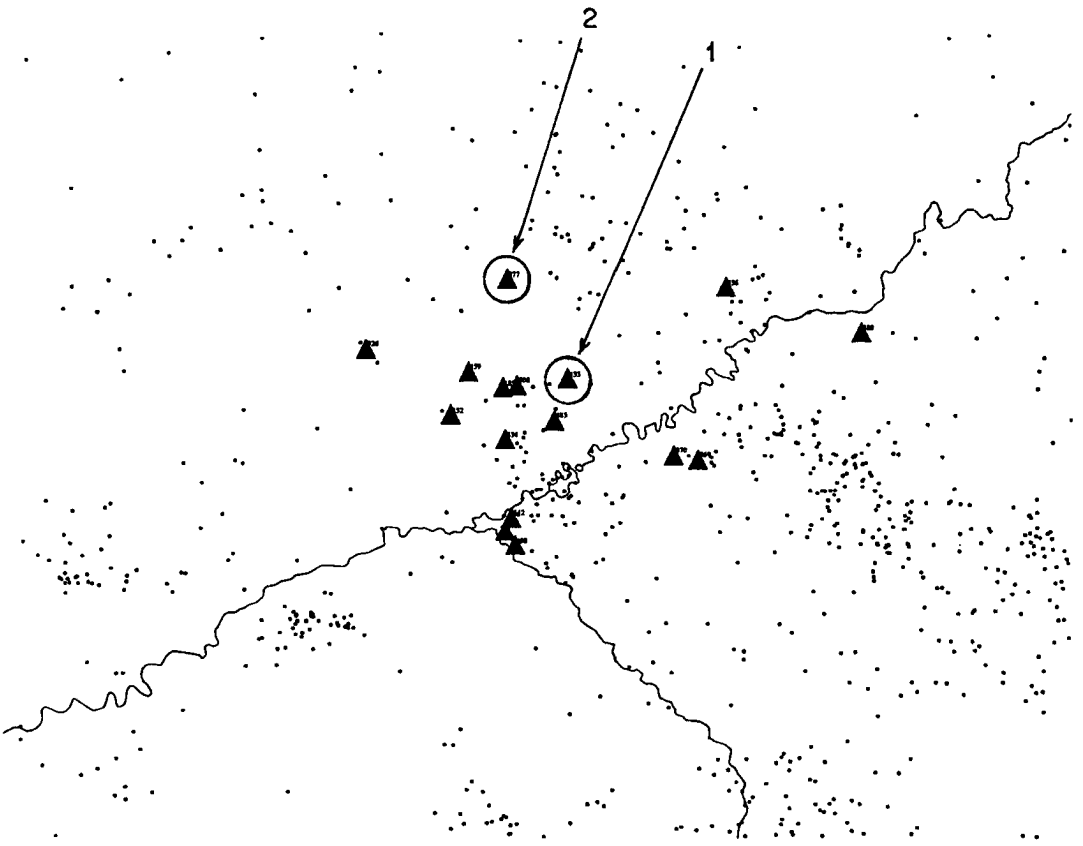

Figure 6.6: Lightning strike map of study area after Julian day 197.

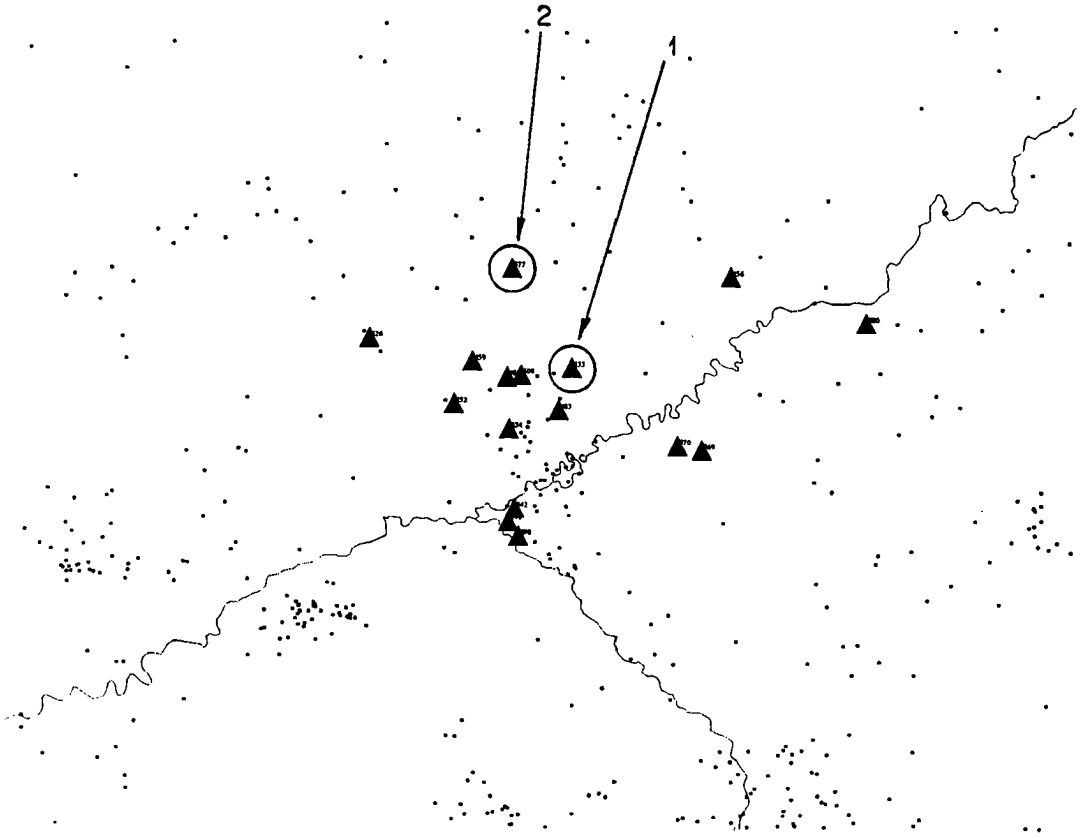

Figure 6.7: Lightning strike map of study area up to 30 days after Julian day 197.

Chapter 7

SUMMARY AND CONCLUSIONS

7.1 Summary

The primary goal of this study was to demonstrate how differences in surface albedo can lead to the development of mesoscale circulations similar in strength to the classical sea-breeze circulation. Once proven that a circulation center could develop, additional effort was used to show that the center was capable of developing clouds to a point where the cloud could become capable of producing precipitation, and possibly lightning. Lightning is the main cause of forest fires in Alaska, so the possibility that forest fire burn areas could lead to more forest fires would be of great interest to the fire management authorities in Alaska.

The low density of observational sites in Alaska made the gathering of any definitive evidence of mesoscale circulations. This necessitated the use of RAMS to simulate the mesoscale circulations and their subsequent effects on the atmosphere. The model was initialized with an actual Fairbanks, Alaska sounding and configured to predict several atmospheric variables: vertical velocities across the burn areas, vertical velocities near the maximum strength of the circulation centers, horizontal winds and temperatures near the surface, cloud water mixing ratios, and precipitation amounts (if any). Two fires near the small town of Fort Yukon that occurred during the summer of 1988 were used as study cases. Both fires were large, with the first fire consuming over 400 square kilometers of woodland, and the second consuming over 100 square kilometers of woodland. RAMS simulations used a single grid covering 6400 square kilometers with a 2 km grid increment. The small grid increments along with the use of full microphysics was used to obtain as accurate as possible the prediction of possible cloud formation and precipitation. The USGS 10 minute topography was also used.

Both simulations of the case studies produced the hypothesized mesoscale circulations, with the first case producing the strongest upward vertical velocities. Strong upward vertical velocities also developed with diurnal heating along the higher terrain. Horizontal winds near the surface were stronger in the first case, while near surface temperatures were much higher in the second case. The first case study generated sufficient water vapor to produce visible clouds. Measurable simulated rainfall was also produced by the clouds in the first case. The second case generated a few scattered clouds over the higher terrain. When the simulations were run without the burn-area albedo modifications, the only circulation centers to form were associated with the upslope flow near the higher terrain and normal heating of the surface terrain in the river valley. There also were no organized areas of clouds or precipitation in the unmodified simulations, although some scattered clouds were simulated along with some light precipitation. A look at sensible heat flux also showed the effects of the lower albedo burn area, with enhanced flux values in and near the burn area.

Several sensitivity simulations were run to show the possible effects of burn area size, surface albedo, geostrophic wind speed and direction, and thermodynamic stability on upward vertical velocities, circulation size, and circulation location. The strongest upward vertical velocities were generated by the 400 square kilometer burn area (Case 1a) as opposed to the 100 square kilometer burn area (Case 1b). The vertical extent of the circulation center was also greater in Case 1a, while circulation locations were similar. Horizontal winds near the surface showed the effects of the circulation center, converging in the area where upward vertical velocities were the strongest as required by mass continuity. Potential temperatures also showed the effects of the circulation center, with the lowest temperatures measured near the center of the circulation center. When a burn area albedo of 0.05 (Case 2a) was used, the generated mesoscale circulation was stronger than the 0.10 albedo (Case 2b) run. The vertical extent and location were similar for both cases. Winds and potential temperature fields were similar to those results obtained in cases 1a-b. The strongest upward vertical velocities for the geostrophic wind runs were obtained in the 0.0 m s^{-1} run. The weakest upward vertical velocities were

obtained in the 5.0 m s^{-1} run. The 2.5 m s^{-1} and -2.5 m s^{-1} runs fell in between the 0.0 m s^{-1} and 5.0 m s^{-1} runs. Horizontal winds and potential temperature fields followed the same trend, with the strongest winds and coolest temperatures associated with the 0.0 m s^{-1} run. The thermodynamic stability sensitivity runs had the strongest upward vertical velocities associated with the 2.5°C case. The 9.0°C had only very weak upward velocities. Horizontal winds and potential temperature fields followed a similar pattern.

Actual observational data was limited to lightning strikes collected by the Alaskan lightning detection network. Plots of lightning strikes during the summer of 1988 showed patterns of concentration in and near the higher terrain. Plots of lightning strikes after the fires showed patterns of concentration not only in and near the higher terrain, but also near the burn areas. These patterns continued until the end of the storm season.

7.2 Conclusions

The study of burn areas in Alaskan interior and their possible effect on the surrounding area produced some very interesting results. Not only did the model produce a mesoscale circulation similar in strength to a sea-breeze circulation, but it also produced clouds and precipitation. Sensitivity runs and plots of lightning strikes also support this conclusion. Based on the results of the two case studies and the sensitivity runs, the following conclusions can be made.

- An increase in the size of the burn area results in an increase in the upward vertical velocities associated with the circulation center. This is primarily due to the larger area being able to develop a more developed circulation center.

- Lowering the albedo for a burn area results in an increase in the upward vertical velocities associated with the circulation center. The more destructive the burn, the lower the surface albedo and the stronger the upward vertical velocities. This is due to the sharp boundary layer thermal differences between the burned and unburned land areas. A look at the sensible heat flux fields also demonstrated this.

- Geostrophic winds over 2.5 m s^{-1} cause a rapid weakening in the size and strength of the circulation center. The weakest upward vertical velocities are associated with the synoptic flow being $\geq$ 5.0 m s^{-1}. This is due to the horizontal pressure gradient generated by the differential heating being insufficient to overcome the kinetic energy of the large-scale flow.

- Stability conditions have a significant effect on the strength of the circulation center. The more stable the sounding, the weaker the circulation center. A weakly stratified atmosphere allows for stronger upward vertical velocities.

- There is a minimum size to the burn area before a cloud can form. Burn areas over 400 square kilometers in size generated clouds, while burn areas under 150 square kilometers did not.

- There also is a minimum albedo needed to generate clouds. From the sensitivity runs, it appears that burn areas with an albedo of 0.10 or higher would not generate clouds. This is due to the much weaker upward vertical velocities in the circulation center.

- Burn areas located near/on higher terrain could have a major effect on the upslope flow that typically happens during the day. The albedo difference would act to invigorate the upslope flow through the increased heating.

Finally, when the lightning plots are used, the following conclusions can be made:

- The large burn areas are capable of producing mesoscale circulation centers strong enough to produce clouds and possible precipitation. This also includes the potential to produce lightning.

- The generation of any convection in/near the burn area would also result in an increase in electrical activity. This would mainly be downwind of the burn area or in the higher terrain surrounding the study area.

- Generation of convection would depend on the severity of the burn area. Heavily burned areas could continue to have an effect on the surrounding area for 3-5 years, since the albedo difference would persist for this time period. A lightly burned area would only have an effect for one year. Also, there is evidence of prior fires in the area. These prior fire burn areas could act to have a cumulative effect on the area.

7.3 Suggestions for Future Research

Areas of future research are many. Just of few of many are listed below.

- Increase the timescale. Look at fires and lightning data over the last 5 years. The size and severity of a fire could be compared to the available lightning data. This would also let one look at follow-up fires. Follow-up fires would help to prove that one forest fire could lead to future forest fires. By looking at previous fire and burn data, one could see if all of the fires had a cumulative effect on the generation of convection in the area.

- Use AVHRR and LANDSAT imagery to observe any actual generation of clouds in the vicinity of the burn areas. This could include looking for persistent cumulus any cloud areas downwind of the burn areas and the enhancement of any existing clouds.

- Set up a network of wind, temperature, and rain sensors in and near to several of the burn areas. These measurements would provide more observational evidence to the existence of the mesoscale circulations.

- Study the effects of burn areas on the enhancement of any existing convection. This would require the use of satellite and radar.

- Look at other areas where large fires occur, including the Yellowstone Park area, the Amazon River valley, and the Canadian interior. Model simulations of these areas would be interesting.

REFERENCES

Anthes, R.A., 1978: The height of the planetary boundary layer and the production of circulation in a sea breeze model. *J. Atmos. Sci.*, **35**, 1231- 1239.

Anthes, R.A, 1984: Enhancement of convective precipitation by mesoscale variations in vegetative covering in semiarid regions. *J. Climate Appl. Meteor.* **23**, 541-554.

Arritt, R.W., 1993: Effects of the large-scale flow on characteristic features of the sea breeze. *J. Appl. Meteor.*, **32**, 116-125.

Atkinson, B.W., 1981: *Meso-scale atmospheric circulations.* Academic Press, London.

Avissar, R. and R.A. Pielke, 1991: The impact of plant stomatal control on mesoscale atmospheric circulations. *Agric. Forest Meteor.*, **54**, 353-372.

Baughman, R.G., and C.W. Schmid, 1977: Alaskan lightning storm characteristics. USDA Forest Service Research Note INT-235, 6 pgs.

Chen, S., and W.R. Cotton, 1983: A one-dimensional simulation of the strato-cumulus-capped mixed layer. *Bound. Layer. Meteor.*, **25**, 289-321.

Cram, Jennifer M., 1990, Ph.D. Dissertation: Numerical simulation and analysis of the propagation of a prefrontal squall line. Department of Atmospheric Science, Colorado State University, 332 pp.

Flannigan, M.D., and B.M. Wotton, 1991: Lightning-ignited forest fires in northwestern Ontario. *Can. J. Forest Res.*, **21**, 277-287.

Flatau, P.J., G.J. Tripoli, J. Verlinde, and W.R. Cotton, 1989: The CSU-RAMS Cloud Microphysics Model: General theory and code documentation. Department of At-

mospheric Science, Colorado State University, Atmospheric Science Paper No. 451, 88 pp.

Fuquay, D.M., R.G. Baughman, A.R. Taylor, and R.G. Hawe, 1967: Characteristics of seven lightning discharges that have caused forest fires. *J. Geophys. Res.*, **72(24)**, 6371-6373.

Fuquay, D.M., A.R. Taylor, R.G. Hawe, and C.W. Schmid Jr., 1972: Lightning discharges that have caused forest fires. *J. Geophys. Res.*, **77(12)**, 2156-2158.

Fuquay, D.M., R.G. Baughman, and D.J. Latham, 1979: A model for predicting lightning fire ignitions in wildlands fuels. USDA Forest Service Research Paper INT-217.

Gale Research Company, 1981: *Weather of U.S. Cities, Volume I, City Reports, Alabama-Missouri.*, Gale Research Company, Book Tower, Detroit Michigan, 1-494.

Johnson, R.H., G.S. Young, J.J. Toth, and R.M. Zehr, 1984: Mesoscale weather effects of variable snow cover over northeast Colorado. *Mon. Wea. Rev.*, **112**, 1141-1152.

Klemp, J.B., and R.B. Wilhelmson, 1978: The simulation of three-dimensional convective storm dynamics. *J. Atmos. Sci.*, **35**, 1070-1096.

Komarek, E.V., 1976: Fire: Control, ecology, and management. *Fire Management in the Northern Environment Symposium*, Bureau of Land Management, 48-78.

Kuo, H.L., 1974: Further studies of the parameterization of the influence of cumulus convection on the large-scale flow. *J. Atmos. Sci.*, **31**, 1232-1240.

Louis, J.F., 1979: A parametric model of vertical eddy fluxes in the atmosphere. *Bound.-Layer Meteor.*, **17**, 187-202.

Lyons, W.A., and H.S. Cole, 1976: Photochemical oxidant transport: Mesoscale lake breeze and synoptic-scale aspects. *J. Appl. Meteor.*, **15**, 733-743.

Mahfouf, J.F., E. Richard, and P. Mascart, 1987: The influence of soil and vegetation on the development of mesoscale circulation. *J. Climate Appl. Meteor.*, **26**, 1483-1495.

Martin, C.L. and R.A. Pielke, 1983: The adequacy of the hydrostatic assumption in sea breeze modeling over flat terrain. *J. Atmos. Sci.*, **40**, 1472-1481.

McCumber, M., April, 1980, Ph.D. Dissertation: A numerical simulation of the influence of heat and moisture fluxes upon mesoscale circulations. University of Virginia, Charlottesville, 255 pgs.

Mesinger, F., and A. Arakawa, 1976: Numerical methods used in atmospheric models. GARP Publication Series, No. 14, WMO/ICSU Joint Organizing Committee, 69 pp.

Molinari, J., and T. Corsetti, 1985: Incorporation of cloud scale and mesoscale down-drafts into a cumulus parameterization: Results of one and three-dimensional integrations. *Mon. Wea. Rev.*, **13**, 485-501.

Morris, W.G., 1934: Lightning storms and fires on the National Forests of Oregon and Washington., USDA Forest Service Research Note, 27 pgs.

Papineau, J., 1992, M.S. Thesis: A performance evaluation of the NGM and RAMS models for the 29-30 March 1991 Front Range storm. Department of Atmospheric Science, Colorado State University, 73 pp.

Pielke, R.A. and R. Avissar, 1990: Influence of landscape structure on local and regional climate. *Landscape Ecology*, **4**, 133-155.

Pielke, R.A. and X. Zeng, 1989: Influence on severe storm development of irrigated land. *Natl. Wea. Dig.*, **14**, 16-17.

Pielke, R.A., G. Dalu, J.R. Garratt, T.G.F. Kittel, R.A. Stocker, T.J. Lee, and J.S. Snook, 1990: Influence of mesoscale landuse on weather and climate and its representa-

tion for use in large scale models. Indo-U.S. Seminar on "The Parameterization of Subgrid-Scale Processes in Dynamical Models of Medium-Range Prediction and Global Climate", Pune, India. August 6-10, 1990, Wiley Eastern Limited, 537-586.

Pielke, R.A., W.R. Cotton, R.L. Walko, C.J. Tremback, M.E. Nicholls, M.D. Moran, D.A. Wesley, T.J. Lee, and J.H. Copeland, 1992: A comprehensive meteorological modeling system – RAMS. *Meteor. Atmos. Phys.*, **49**, 69-91.

Rodriguez, Humberto, 1992, M.S. Thesis: Influence of mesoscale variations in land surface albedo on large-scale averaged heat fluxes. Department of Atmospheric Science, Colorado State University, 70 pp.

Rotunno, R., 1983: On the linear theory of the land- and sea-breeze. *J. Atmos. Sci.*, **40**, 1999-2005.

Rowe, J.S., 1976: Large fires in the large landscapes of the North. *Fire Management in the Northern Environment Symposium*, Bureau of Land Management, 8-32.

Segal, M., and R.W. Arritt, 1992: Nonclassical mesoscale circulations caused by surface sensible heat-flux gradients. *Bull. Amer. Meteor. Soc.*, **73**, 1593-1604.

Segal, M., R. Avissar, M.C. McCumber, and R.A. Pielke, 1988: Evaluation of vegetation effects on the generation and modification of mesoscale circulations. *J. Atmos. Sci.*, **45**, 2268-2292.

Segal, M., W. Schreiber, G. Kallos, R.A. Pielke, J.R. Garratt, J. Weaver, A. Rodi, and J. Wilson, 1989: The impact of crop areas in northeast Colorado on midsummer mesoscale thermal circulations. *Mon. Wea. Rev.*, **117**, 809-825.

Segal, M., J.R. Garratt, R.A. Pielke, and Z. Ye., 1991a: Scaling and numerical model evaluation of snow-cover effects on the generation and modification of daytime mesoscale circulations. *J. Atmos. Sci.*, **48**, 1024-1042.

Segal, M., J.H. Cramer, R.A. Pielke, J.R. Garratt, and P. Hildebrand, 1991b: Observational evaluation of the snow-breeze. *Mon. Wea. Rev.*, **119**, 412-424.

Song, J.L., R.A. Pielke, M. Segal, R.W. Arritt, and R. Kessler, 1985: A method to determine non-hydrostatic effects within subdomains in a mesoscale model. *J. Atmos. Sci.*, **42**, 2110-2120.

Tremback, C.J., and R. Kessler, 1985: A surface temperature and moisture parameterization for use in mesoscale numerical models. *Preprints, 7th AMS Conference on Numerical Weather Prediction*, June 17-20, Montreal, Quebec, Canada, Amer. Meteor. Soc., Boston, 433-434.

Tremback, C.J., G.J. Tripoli, and W.R. Cotton, 1985: A regional scale atmospheric numerical model including explicit moist physics and a hydrostatic time-split scheme. *Preprints, 7th AMS Conference on Numerical Weather Prediction*, June 17-20, Montreal, Quebec, Canada, Amer. Meteor. Soc., Boston, 433-434.

Tremback, C.J., J. Powell, W.R. Cotton, and R.A. Pielke, 1985: The forward-in-time upstream advection scheme: Extension to higher orders. *Mon. Wea. Rev.*, **115**, 540-555.

Tripoli, G.J., and W.R. Cotton, 1982: The Colorado State University three- dimensional cloud/mesoscale model - 1982: Part I: General theoretical framework and sensitivity experiments. *J. De Rech. Atmos.*, **16**, 185-220.

Viereck, L.A., and C.T. Dyrness, 1979: Ecological effects of the Wickersham Dome fire near Fairbanks, Alaska. USDA Forest Service General Technical Report PNW-90, 71 pgs.

Watson, C.E., 1974: *Climates of the States, Volume II, Western States Including Alaska and Hawaii.* Water Information Center, Port Washington, New York, 484-975.

Xian, Zejin, 1991, M.S. Thesis: A 2-D model study of the influence of the surface on mesoscale convection during the Indian monsoon. Department of Atmospheric Science, Colorado State University, 110 pp + appendix.

Xian, Z. and R.A. Pielke, 1991: The effects of width of land masses on the development of sea breezes. *J. Appl. Meteor.*, **30**, 1280-1304.

Yan, H., and R.A. Anthes, 1988: The effect of variations in surface moisture on mesoscale circulations. *Mon. Wea. Rev.*, **116**, 192-208.